

Abstract

**Measurement of total hadronic differential cross
sections in the LArIAT experiment**

Elena Gramellini

2018

Abstract goes here. Limit 750 words.

Measurement of total hadronic differential cross sections in the LArIAT experiment

A Dissertation
Presented to the Faculty of the Graduate School
of
Yale University
in Candidacy for the Degree of
Doctor of Philosophy

by
Elena Gramellini

Dissertation Director: Bonnie T. Fleming

Date you'll receive your degree

Copyright © 2017 by Elena Gramellini

All rights reserved.

Contents

Acknowledgements	v
0 Liquid Argon Detectors at the Intensity Frontier	1
0.1 The Liquid Argon Time Projection Chamber Technology	1
0.1.1 TPCs, Neutrinos & Argon	1
0.1.2 LArTPC: Principles of Operation	3
0.1.3 Liquid Argon: Ionization Charge	6
0.1.4 Liquid Argon: Scintillation Light	10
0.1.5 Signal Processing and Event Reconstruction	13
0.2 The Intensity Frontier Program	16
0.2.1 SBN: Neutrino Interaction and Detection	16
0.2.2 DUNE: Rare Decay Searches	16
0.2.3 Enabling the next generation of discoveries: LArIAT	17
1 LArIAT: Liquid Argon In A Testbeam	20
1.1 The Particles Path to LArIAT	20
1.2 LArIAT Tertiary Beam Instrumentation	23
1.2.1 Bending Magnets	23
1.2.2 Multi-Wire Proportional Chambers	25
1.2.3 Time-of-Flight System	27
1.2.4 Punch-Through and Muon Range Stack Instruments	28

1.2.5	LArIAT Cosmic Ray Paddle Detectors	30
1.3	In the Cryostat	31
1.3.1	Cryogenics and Argon Purity	31
1.3.2	LArTPC: Charge Collection	34
1.3.3	LArTPC: Light Collection System	37
1.4	Trigger and DAQ	40
1.5	Control Systems	41
2	Hadron Interactions in Argon: Cross Section	47
2.1	How to Measure a Hadron Cross Section in LArIAT	47
2.1.1	Event Selection	48
2.1.2	Wire Chamber to TPC Match	50
2.1.3	The Thin Slice Method	51
2.1.4	Procedure testing with truth quantities	54
A	Measurement of LArIAT Electric Field	57

Acknowledgements

A lot of people are awesome, especially you, since you probably agreed to read this when it was a draft.

Chapter 0

Liquid Argon Detectors at the Intensity Frontier

In the next few years, LArTPCs will be the tools to answer some of the burning questions in neutrino physics today. This section illustrates the operational principles of this detector technology, as well as the scope of the key detectors in the US liquid argon program – SBN, DUNE and LArIAT.

0.1 The Liquid Argon Time Projection Chamber Technology

0.1.1 TPCs, Neutrinos & Argon

David Nygren designed the first Time Projection Chamber (TPC) in the late 1970s [18] for the PEP-4 experiment, a detector apt to study electron-positron collisions at the PEP storage ring at the SLAC National Accelerator Laboratory. From the original design in the seventies – a cylindrical chamber filled with methane gas – the TPC detector concept has seen many incarnations, the employment of several different active media and a variety of different particle physics applications, including, but

not limited to the study of electron/positron storage rings (e.g. PEP4, TOPAZ, ALEPH and DELPHI), heavy ions collisions in fixed target and collider experiments (e.g. EOS/HISSL and ALICE), dark matter (ArDM), rare decays and capture (e.g. TRIUMF, MuCap), neutrino detectors and nucleon decay (ICARUS, SBN, DUNE), and neutrino less double beta decay (Next). A nice review of the history of TPCs and working principles is provided in [15].

Several features of the TPC technology make these detectors a more versatile tool compared to other ionization detectors and explain such a wide popularity. TPCs are the only electronically read detector which deliver simultaneous three-dimensional track information and a measurement of the particle energy loss. Leveraging on both tracking and calorimetry, particle identification (PID) capabilities are enhanced over a wide momentum range.

Historically, the active medium in ionization detectors has been in the gaseous form. Carlo Rubbia first proposed the use of a Liquid Argon TPC for a neutrino experiment, ICARUS [20], in 1977. Using nobles elements in the liquid form for neutrino detectors is advantageous for several reasons. The density of liquids is \sim 1000 times greater than gases, increasing the number of target centers for neutrino's interaction in the same volume. Since the energy loss of charged particle is proportional to the target material density, as shown in the Bethe-Block equation, eq. 1, the increased density reflects into a proportionally higher energy loss, enhancing the calorimetry capability of detectors with a liquid active medium. Additionally, the ionization energy of liquids is smaller than gasses by the order of tens of eV. Thus, at the passage of charged particles, liquid generally produce more ionization electrons than gas for the same deposited energy and force the particles to deposit more energy in a shorter range. The downside of using noble liquid gasses in experiments is that they require expensive cryogenic systems to cool the gas until it transitions to its the liquid form. The properties of liquid argon in comparison liquid xenon – a popular choice for dark

Element	LAr	LXe
Atomic Number	18	54
Atomic weight A	40	131
Boiling Point Tb at 1 atm	87.3 K	165.0 K
Density	1.4 g/cm ³	3.0 g/cm ³
Radiation length	14.0 cm	2.8 cm
Moliere Radius	10.0 cm	5.7 cm
Work function	23.6 eV	15.6 eV
Electron Mobility at $E_{field} = 10^4$ V/m	0.047 m ² /Vs	0.22 m ² /Vs
Average dE/dx MIP	2.1 MeV/cm	3.8 MeV/cm
Average Scintillation Light Yield	40000 γ /MeV	42000 γ /MeV
Scintillation λ	128 nm	175 nm

Table 1: LAr, LXe summary of properties relevant for neutrino detectors.

matter and neutrinoless double beta decay detectors – are summarized in table 1. Albeit xenon would be more desirable than argon given some superior properties such as lower ionization energy and higher density and light yield, argon relative abundance abates the cost of argon compared to xenon, making argon a more viable choice for the construction of kilo-ton scale neutrino detectors.

LArTPCs are some times referred as to “electronic” bubble-chambers, for the similarity in the tracking and energy resolution which is coupled with an electronic readout of the imaging information in LArTPCs. Compared to these historic detectors however, LArTPC bestow tridimensional tracking and a self triggering mechanism provided by the scintillation light in the noble gas. An event display of a ν_μ CC interaction candidate in the MicroBooNE detector is shown in picture 1 to display the level of spatial details these detectors are capable of; the color scale of the image is proportional to the energy deposited, hinting to the calorimetry capabilities of the detectors.

0.1.2 LArTPC: Principles of Operation

To the bare bones, a LArTPC is a bulk of liquid argon sandwiched in a flat capacitor, equipped with a light collection system. A uniform electric field of the order of

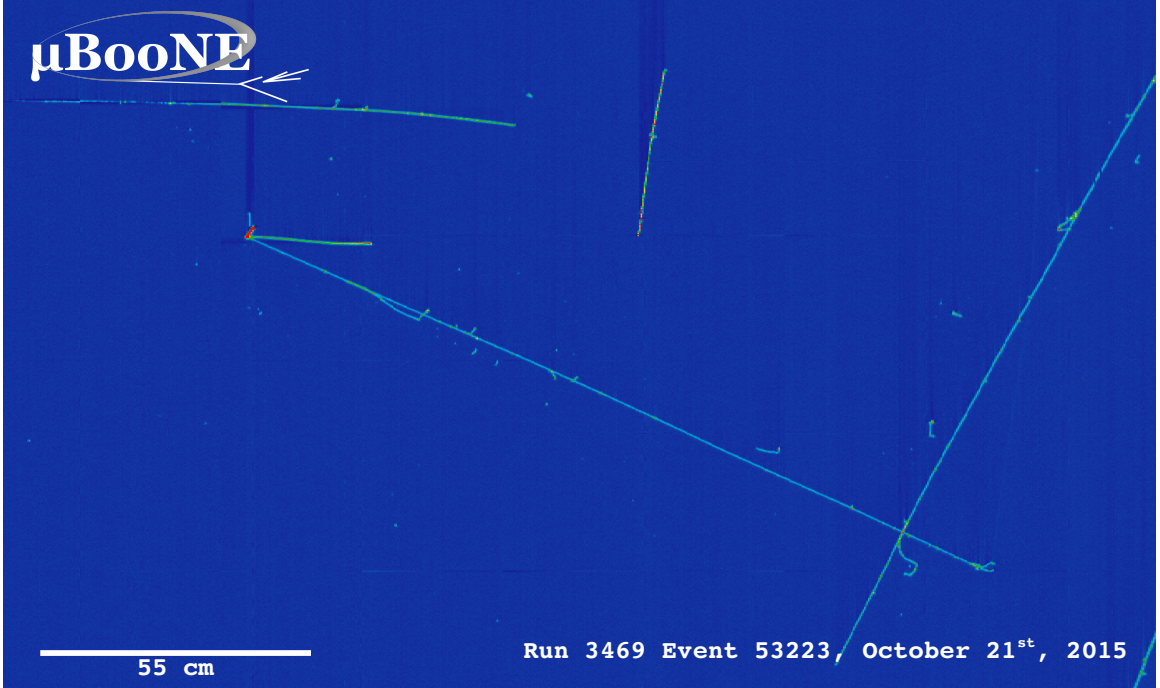


Figure 1: Event display of a ν_μ CC interaction candidate in the MicroBooNE detector.

500 V/cm is maintained constant between the faces of the capacitor. The anode is sensitive to ionization charge and it is usually made of two or more planes segmented into several hundreds parallel sense wires a few millimeters apart; different geometries for the anode segmentation are under study [8].

Argon ionization and scintillation are the processes leveraged to detect particles in the LArTPC active volume. When a ionizing radiation traverses the argon active volume it leaves a trail of ionization electrons along its trajectory and it excites the argon producing of scintillation light – details on the production and detection of ionization charge and scintillation light are provided in 0.1.4 and 0.1.4 respectively. The optical the detector sees the argon scintillation light in matters of nanoseconds. This flash of light determines the start time of an event in the chamber, t_0 . The uniform electric field drifts the ionization electrons from the production point towards the anode in order of hundreds of microseconds or more depending on the chamber dimensions¹. The anode sense wires see either an induced current by the drifting

1. The ionized argon also drifts, but in the opposite directions compared to the electrons. Since

charge (on induction planes) or an injection of the ionization charge (collection plane). An appropriate choice of the voltage bias on each wire plane assures ideal charge transparency, so that all the ionization charge is collected on the collection plane and none on the induction planes.

The arrival time of the charge on the anode sense wires is used to measure the position of the original ionizing radiation in the drift direction. In fact, since the constant electric field implies that the drift velocity is also constant, the position of the original ionization is simply given by the multiplication of the drift velocity by the drift time, where the “drift time” is the difference between t_0 and the charge arrival time on the wire planes. The spacial resolution on this dimension is limited by the time resolution of the electronics or by longitudinal diffusion of the electrons. The spatial information on the different wire planes maps a bi-dimensional projection of the interaction pattern in the plane perpendicular to the drift direction. The spacial resolution on this dimension is limited by the transverse electron diffusion in argon and by the grain of the anode segmentation, i.e. the spacing between the wires in the sense planes [7]. The off-line combination of the 2-D information on the wire planes with the timing information allows for the 3D reconstruction of the event in the chamber.

Since the charge deposited by the ionizing radiation is proportional to the deposited energy and the charge collected on the sense plane is a function of the deposited charge, LArTPC allow the measurement of the energy deposit in the active volume. Effects due to the presence of free charge and impurities in the active volume, such as a finite electron lifetime, recombination and space charge, complicate the relationship between deposited and collected charge affecting the measurement of the particle’s energy, as described in the next section.

the drift time is proportional to the particle mass, the ions’ drift time is much longer than the electrons’. Ionized argon is collected on the cathode which is not instrumented, so it is not used to infer information about the interactions in the chamber.

0.1.3 Liquid Argon: Ionization Charge

The mean rate of energy loss by moderately relativistic elementary charge particles heavier than electrons is well described by the modified Bethe-Bloch [19] equation

$$-\frac{dE}{dx} = K z^2 \frac{Z}{A} \varrho \frac{1}{\beta^2} \left[\frac{1}{2} \ln \frac{2m_e c^2 \beta^2 \gamma^2 T_{max}}{I^2} - \beta^2 - \frac{\delta}{2} \right], \quad (1)$$

where z is the number of unit charge of the ionizing radiation, Z , A and ϱ are the atomic number, mass number and density of the medium, m_e is the electron mass, $\gamma = \frac{\beta}{\sqrt{1-\beta^2}}$ is the Lorentz factor of the ionizing radiation, T_{max} is the maximum kinetic energy which can be imparted to a free electron in a single collision, I is the mean excitation energy on eV, δ is the density correction and $K = 0.307075 \text{ MeV g}^{-1} \text{ cm}^2$ is a numerical conversion factor. The Bethe-Bloch treats as an uniform and continuous process the energy loss by an ionizing radiation via quantum-mechanical collisions producing ionization or an excitation in the medium. The density correction terms becomes relevant for incident particle with high energy, where screening effects due to the polarization of the medium by high energy particles occur.

Excitation and ionization of the detector medium occur in similar amounts. Since the ionizing collisions occur randomly, we can parametrize their number k in a segment of length s along the track with a Poissonian function

$$P(k) = \frac{s^k}{k! \lambda^k} e^{-s/\lambda}, \quad (2)$$

where $\lambda = 1/N_e \sigma_i$, with N_e being the electron density of σ_i the ionization cross-section per electron. About 66% of the ionizing collisions in Argon produce only a single electron/ion pair [15]; in the other cases, the transferred kinetic energy is enough for the primary electron to liberate one or more secondary electrons, which usually stay close to the original pair. Occasionally, electrons can receive enough energy to

be ejected with high energy, forming so-called “ δ -ray”: a detectable ionization short track off the particle trajectory, as shown in figure [ADD figure](#). The average number of δ -ray with energy $E > E_0$ per cm follows the empirical form

$$P(E > E_0) \sim \frac{y}{\beta^2 E_0}, \quad (3)$$

where y is an empirical factor depending on the medium (0.114 for gaseous Ar), and β is v/c .

Purity & Electron Life Time

The presence of electronegative contaminants in liquid argon, such as oxygen and water, is particularly pernicious, since these molecules quench the charge produced by the ionizing radiation. Thus, amount of charge per unit of length dQ/dx collected on the collection plane depends on the charge’s production point in the detector: a ionization produced close to the cathode will see more impurities along its journey to the collection plane than ionization produced close to the anode, resulting in greater attenuation. As a result, the amount of charge collected on the sense wires as a function of the traveled distance follows an exponential decay trend. The traveled distance is generally measured in terms of drift time and the characteristic time constant of the exponential decay is called electron lifetime τ_e . Figure ?? shows the typical life time for LArIAT data [cite technote](#). LArIAT small drift distance (47 cm) allows for a relatively short electron life time. The life time for bigger detectors such as MicroBooNE, whose drift distance is 2.5 m, needs to be of the order of to allow charge collection usable for physics analyses. Energy reconstruction in LArTPC applies a correction for the finite lifetime to calibrate the detector calorimetric response; details for LArIAT are provided in Section ??.

LArTPCs use hermetically sealed and leak-checked vessels to abate the leakage

and diffusion of contaminants into the system. The liquid argon filling of the volume occurs after the vessel is evacuated or purged with gaseous argon [205] to reduce remaining gases in the volume. Even so, the construction of a pure tank of argon is unviable, as several sources of impurity remain. In particular, impurities can come from the raw argon supply, the argon filtration system and from the outgassing from internal surfaces. Outgassing is a continuous diffusive process producing contaminants, especially water, even after the vessel is sealed, particularly from materials in the ullage region². Since research-grade argon comes from the industrial distillation of air, the impurities with the highest concentration are nitrogen, oxygen and water, generally maintained under the 1 part per million level by the vendor. Even so, a higher level of purity is necessary to achieve a free electron life time usable in meter scale detectors. Thus, argon is constantly filtered in the cryogenic system, which reduce the oxygen and water contamination to less than 100 parts per trillion. The filtration system depends on the size and drift distance of the experiment and, for experiments on several meters scale, it includes an argon recirculation system.

Recombination Effect

After production, ionization electrons thermalize with the surrounding medium and may recombine with nearby ions. Recombination might occur either between the electron and the parent ion through Coulomb attraction (Onsager geminate theory [2]) or thanks to the collective charge density of electrons and ions from multiple ionizations in a cylindrical volume surrounding the particle trajectory (Jaffe[3] columnar model). Consideration on the average electron-ion distance and the average ion-ion distance for argon show that the probability of geminate recombination is low; thus recombination in argon is mainly due to collective effects [1]. Since protons, kaons

2. . While the liquid argon low temperature reduces outgassing in the liquid, this process remains significant for absorptive material (such as plastic) above the surface of the liquid phase

and stopping particles present a higher ionization compared to MIPs, recombination effects are more prominent when considering the reconstruction of energy deposited by these particles.

Models for a theoretical descriptions of recombination base on are provided in (Birks model [6]) and in (Box model [7]). The Birks model assumes a gaussian spatial distribution around the particle trajectory during the entire recombination phase and identical charge mobility for ions and electrons. The Box model also assumes that electron diffusion and ion mobility are negligible in liquid argon during recombination In these models, the fraction of ionization electrons surviving recombination is a function of the number of ion-electron pairs per unit length, the electric field, the average ion-electron separation distance after thermalization and the angle of the particle with respect to the direction of the electric field – plus the diffusion coefficient in the Birks model. Given the stringent assumptions, it is perhaps not surprising that these models are in accordance to data only in specific regimes: the Birks model is generally used to describe recombination for low dE/dx , the Box model for high $dEdX$. In LArTPC, the ICARUS and ArgoNeut have measured recombination in [8] and [1] respectively. Since LArIAT uses the refurbished ArgoNeut TPC and cryostat, LArIAT currently corrects for recombination using the ArgoNeut measurement, shown in figure [find figure](#).

Space Charge Effect

Slow-moving positive argon ions created during ionization can build-up in LArTPC, causing the distortion of the electric field within the detector. This effect, called “space charge effect” leads to a displacement in the reconstructed position of the signal ionization electrons. In surface LArTPCs the space charge effect is primarily due to the rate of ionization produced by cosmic rays which is slowly drifting in the chamber at all times. Surface LArTPC of the size of several meters are expected

to be modestly impacted from the space charge effect, where charge build-up creates anisotropy of the electric field magnitude of the order of 5% at a drift field of 500 V/cm. The smallness of the LArIAT drift volume is such that effect of space charge on the electric field is expected to be even smaller. **CHIEDI A FLAVIO**

0.1.4 Liquid Argon: Scintillation Light

Liquid argon emits scintillation light at the passage of charged particles. LArTPCs leverage this property to determine when the ionization charge begins to drift towards the anode plane.

Scintillation Process

Scintillation light in argon peaks in the ultraviolet at a 128 nm, shown in comparison to Xenon and Krypton in Figure [183]. The light yield collected by the optical detector depends on the argon purity, the electric field, the dE/dx and particle type, averaging at the tens of thousands of photons per MeV. The de-excitation of Rydberg dimers in the argon is responsible for the scintillation light. Rydberg dimers exist in two states: singlets and a triplets. The time constant for the singlet radiative decay is 6 ns, resulting in a prompt component for the scintillation light. The decay of the triplet is delayed by intersystem crossing, producing a slow component with a time constant of ~ 1500 ns. “Self-trapped exciton luminescence” and “recombination luminescence” are the two processes responsible for the creation of the Rydberg dimers. In the first process, a charged particle excites an argon atom which becomes self-trapped in the surrounding bulk of argon, forming a dimer; the dimer is in the singlet state 65% of the times and in the triplet state 35% of the times. In case of recombination luminescence, the charged particle transfers enough energy to ionize the argon. The argon ion forms a charged argon dimer state, which quickly recombines with the thermalized free electron cloud. Excimer states are produced in the recombination,

roughly half in the singlet and half in the triplet state. The light yield dependency on the electric field, on the dE/dx and particle type derives from the role of free charge in the recombination luminescence process. The spacial separation between the argon ions and the free electron cloud depends on the electric field. On one hand, a strong electric field diminishes the recombination probability, leading to a smaller light yield; on the other, it increases the free charge drifting towards the anode plane. Hence, the amount of measurable charge and light anti-correlates as a function of the electric field. Ionizing particles in the argon modify the local density of both free electrons and ions depending on their dE/dx . Since the recombination rate is proportional to the square of the local ionization density, highly ionizing particles boost recombination and the subsequent light yield compared to MIPs. The possibility to leverage this dependency for pulsedshape-based particle identification has been shown in [186], [187].

Effects Modifying the Light Yield

The production mechanism through emission from bound excimer states implies that argon is transparent to its own scintillation light. In fact, the photons emitted from these metastable states are not energetic enough to re-excite the argon bulk, greatly suppressing absorption mechanisms. In a LArTPC however, several processes modify the light yield in between the location where light is produced and the optical detector. In a hypothetical pure tank of argon, Rayleigh scattering would be the most important processes modifying the light yield. Rayleigh scattering changes the path of light propagation in argon, prolonging the time between light production and detection. The scattering length has been measured to be 66 cm [191], shorter than the theoretical prediction of ~ 90 cm [190]; this value is short enough to be relevant for the current size of LArTPCs detectors. In fact, Rayleigh scattering worsen the resolution on t_0 , the start time for charge drifting, and alters the light directionality, complicating the matching between light and charge coming from the same object in

case of multiple charged particles in the detector.

Traces of impurities in argon such as oxygen, water and nitrogen also affect the light yield, mainly via absorption and quenching mechanisms. Absorption occurs as the interaction of a 128 nm photon directly with the impurity dissolved in the liquid argon. Differently, quenching occurs as the interaction of an argon excimer and an impurity, where the excimer transfers its excitation to the impurity and dissociates non-radiatively. Given this mechanism, it is evident how quenching is both a function of the impurity concentrations and the excimer lifetime. Since the triplet states live much longer than the singlet states, quenching occurs mainly on triplet states, affecting primarily the slow component of the light, reducing the scintillation yield and a shortening of the scintillation time constants.

The stringent constraints for the electron life time limit the presence of oxygen and water to such a low level that both absorption and quenching on these impurity is not expected to be significant [210]. Contrarily, the nitrogen level is not bound by the electron life time constraints – nitrogen being an inert gas, expensive to filter. Thus, nitrogen is often present at the level provided by the vendor. The effects of nitrogen on argon scintillation light have been studied in the WArP R&D program and at several test stands. The quenching process induced by nitrogen in liquid Ar has been measured to be proportional to the nitrogen concentration, with a rate constant of $\sim 0.11 \mu\text{s}^{-1} \text{ ppm}^{-1}$; appreciable decreasing in lifetime and relative amplitude of the slow component have been shown for contamination as high as a few ppm of nitrogen [2]. For a nitrogen concentration of 2 parts per million, typical of the current generation of LArTPC, the attenuation length due to nitrogen has been measured to be ~ 30 meters [16].

Wavelength Shifting of LAr Scintillation Light

Liquid argon scintillation light is invisible for most optical detectors deployed in LArTPC, such as cryogenic PMTs and SiPMs, since a wavelength of 128 nm is generally too short to be absorbed from most in glasses, polymers and semiconductor materials. Research on prototype SiPMs absorbing directly VUV light and their deployment in noble gasses experiment is ongoing but not mature [22]. Thus, experiments need to shift the wavelength of scintillation light to be able to detect it. Albeit deployed in different ways, neutrinos and dark matter experiments commonly use 1,1,4,4-tetraphenyl-butadiene (TPB) to shift the scintillation light. TPB, whose chemical structure is shown in figure , absorbs the vacuum ultraviolet (VUV) light and emits in the visible at ~ 425 nm [231], with a ratio of visible photon emitted per VUV photon absorbed of $\sim 1.2:1$ [12].

Neutrino experiments typically coat their optical detector system evaporating a layer of TPB either directly on the PMTs glass surface or on acrylic plates mounted in front of the PMTs [cite microboone](#); this technique allows the fast detection light coming directly from the neutrino interaction. Dark matter experiments typically evaporate TPB on reflective foils mounted on the inside walls of the sensitive volume and detect the light after it has been reflected; this technique leads to a higher and more uniform light yield, though scattering effects for both the visible and VUV light augment the propagation time and hinder directionality information[some DM detector](#) . In order to take advantage of both these techniques, hybrid systems with PMT coating and foils are being considered for the next generation of large neutrino detectors [cite SBND?](#).

0.1.5 Signal Processing and Event Reconstruction

In this section we illustrate the processing and reconstruction chain of the TPC signals, from the pulses on the sense wire to the construction of three dimensional objects

with associated calorimetry.

Deconvolution. Induction and collection planes have different field responses, given the different nature of the signals on these planes: the wires on the induction planes see inductive signal of the drifting charge, while the wires on the collection planes see the current derived from the charge entering the conductor. Thus, signals on the induction plane are bi-polar pulse and signal on the collection plane are unipolar pulses, see Figure [ADD PULSES FIGURE](#). The first step in signal processing is deconvolution, that is a series of off-line algorithms geared towards undoing the detector effects. The result of the deconvolution step is the production of a comparable set waveforms on all planes presenting unipolar, approximately gaussian-like pulses. Signal from all planes are treated on equal footage beyond this point. Some LArTPC apply noise filtering in the frequency domain just after the deconvolution to clean up wire cross talk. Since signals from the LArIAT TPC are extremely clean, noise filtering is not necessary.

Hit Reconstruction. The second stage of the signal processing is the reconstruction of hits, indicating an energy deposition in the detector. A peak finder scans the deconvolved TPC waveforms for each wire on the whole readout time looking for spikes above the waveform’s baseline. It then fits these peaks with gaussian shapes and stores the fit parameters such as the quality of the fit, the peak time, height and area under the gaussian fit. The information resulting from this process a single spike form a single reconstructed “hit”. The next steps in the event reconstruction chain will then decide if rejecting hits with poor fits. It is important to notice how the height and width of the hit depend on the topology of the event: for example, a particle running parallel to the wire planes will leave a series of sharp hits on many consecutive wires, while a particle traveling towards the planes will leave a long, wide

hit on very few wires. The height of the hits and their integral is proportional to the charge collected on the wire, so it depends on the particle type.

The event reconstruction chain uses collection of hits to form more complex objects associated with the particles in the detector. The development of different approaches to accomplish this task is an extremely hot topic in LArTPC event reconstruction which spans from more traditional approaches such as line-clustering [?] [argoneut paper](#) to the use of machine learning tools [?] [KAZU'S paper](#). Generally speaking, the scope of hit clustering and event reconstruction to provide shower-like or track like-objects with an associated energy reconstruction. This is because different particles have different topology in the detector – electrons and photon create electromagnetic showers, resulting in shower-like topologies, while muons and hadrons leave track-like signals. For the scope of these thesis, we will describe only LArIAT's approach to track reconstruction even if we recognize the breath of LArTPC event reconstruction is much wider. We are interested in the reconstruction of pions and kaons in the active volume, whose topology is track-like.

2D Clustering Reconstruction. The LArIAT reconstruction of track-like objects starts by clustering hits on the collection and induction planes separately with the use of the TrajCluster clustering package [?] [Bruce](#). TrajCluster looks for a collection of hits in the wire-time 2D space which can be described with a line-like 2D trajectory. TrajCluster reconstructs trajectories by adding trajectory points to the leading edge of the trajectory while stepping through the 2D space of hits. Several factors determine whether a hit is added to the trajectory, including but not limited to

1. the goodness of the fit of the single hit,
2. the charge of the hit compared to the average charge and RMS of the hits already forming the trajectory,

3. the goodness of trajectory fit with and without the hit addition,
4. the angle between the two lines formed by the collection of hits before and after the considered hit in the trajectory.

3D Track Reconstruction. The 3D tracking set of algorithms uses clusters close in time on the induction and collection planes as starting point to form a 3D track. Firstly, it constructs a tentative 3D trajectory using the edges of the clusters. Then, it projects back the tentative trajectory onto the planes and adjusts the parameters of the 3D track fit such that they minimize the distance between the fit projections and the track hits in all wire planes simultaneously. The track algorithm can use multiple clusters in one plane, but it can never break them in smaller groups of hits. This algorithm was first developed for the ICARUS collaboration [5].

0.2 The Intensity Frontier Program

0.2.1 SBN: Neutrino Interaction and Detection

0.2.2 DUNE: Rare Decay Searches

DUNE will achieve a wide non-accelerator physics program. The key elements for a rare decay experiment are: massive active volume, long exposure, high identification efficiency and low background. Figure 2 shows the current best experimental limits on nucleon decay lifetime over branching ratio (dots). Historically, the dominant technology used in these searches has been water Cherenkov detectors: all the best experimental limits on every decay mode are indeed set by Super-Kamiokande [?, ?]. It is particularly important to notice that the kaon energy for the proton decay mode $p \rightarrow K^+ \bar{\nu}$ is under Cherenkov threshold. Super-Kamiokande set the limit on the lifetime for the $p \rightarrow K^+ \bar{\nu}$ mode by relying on photons from nuclear de-excitation and on the muon tagging in the kaon decay leptonic mode. For this reason, an attractive

alternative approach to identifying nucleon decay is the use of a Liquid Argon Time Projection Chamber (LArTPC).

LArTPCs can complement nucleon decay searches in modes where water Cherenkov detectors are less sensitive, especially $p \rightarrow K^+ \bar{\nu}$. According to [?], DUNE will have an active volume large enough, have sufficient shielding from the surface, and will run for lengths of time sufficient to compete with Hyper-K, opening up the opportunity for the discovery of nucleon decay.

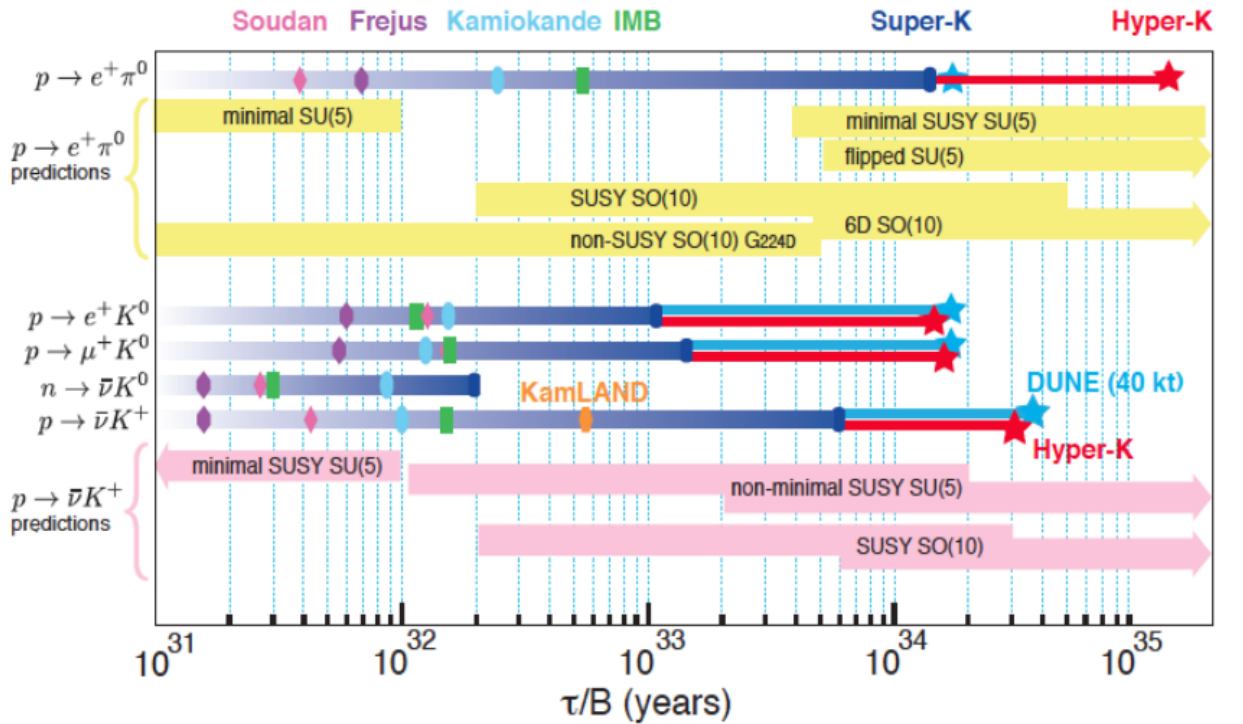


Figure 2: Proton decay lifetime limits from passed and future experiments.

0.2.3 Enabling the next generation of discoveries: LArIAT

LArIAT, a small Liquid Argon Time Projection Chamber (LArTPC) in a test beam, is designed to perform an extensive physics campaign centered on charged particle cross section measurements while characterizing the detector performance for future LArTPCs. LArTPC represents one of the most advanced experimental technologies

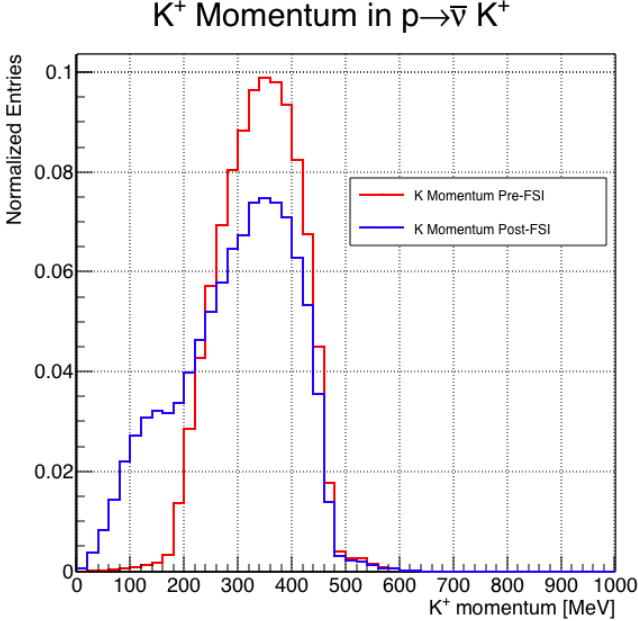


Figure 3: Momentum of the kaon outgoing a proton decay event as simulated by the Genie 2.8.10 event generator in argon. The red line represent the kaon momentum distribution before undergoing the simulated final state interaction inside the argon nucleus, while the blue line represents the momentum distribution after FSI.

for physics at the Intensity Frontier due to its full 3D-imaging, excellent particle identification and precise calorimetric energy reconstruction. This complex technology however needs a thorough calibration and dedicated measurements of some key quantities to achieve the precision required for the next generation of discoveries at the Intensity Frontier which LArIAT can provide.

The LArIAT LArTPC is deployed in a dedicated calibration test beamline at Fermilab. We use the LArIAT beamline to characterize the charge particles before they enter the TPC: the particle type and initial momentum is known from beamline information. The precise calorimetric energy reconstruction of the LArTPC technology enables the measurement of the total differential cross section for tagged hadrons. The Pion-Nucleus and Kaon-Nucleus total hadronic interaction cross section have never been measured before in argon and they are a fundamental step to shed light on light meson interaction in nuclei. Additionally, these measures provides a key in-

put to neutrino physics and proton decay studies in future LArTPC experiments like SBN and DUNE. add paragraph on all wonderful things lariat can do... some event displays would be nice!

ADD genie proton decay kaon distribution and lariat beamline overlaid The signature of a proton decay event in the “LAr golden mode” is the presence of a single kaon of about 400 MeV in the detector.

Chapter 1

LArIAT: Liquid Argon In A Testbeam

In this chapter, we describe the LArIAT experimental setup. We start by illustrating the journey of the charge particles in the Fermilab accelerator complex, from the gaseous thermal hydrogen at the Fermilab ion source to the delivery of the LArIAT tertiary beam at MC7. We then describe the LArIAT beamline detectors, the LArTPC, the DAQ and the monitoring system.

1.1 The Particles Path to LArIAT

LArIAT’s particles history begins in the Fermilab accelerator complex with a beam of protons. The process of protons acceleration develops in gradual stages (see picture 1.1): gaseous hydrogen is ionized in order to form H^- ions; these ions are boosted to 750 keV by a Cockcroft-Walton accelerator and injected to the Linac linear accelerator that increases their energy up to 400 MeV; then, H^- ions pass through a carbon foil and lose the two electrons; the resulting protons are then injected into a rapid cycling synchrotron, called Booster; at this stage, protons reach 8 GeV of energy and are compacted into bunches; the next stage of acceleration is the Main Injector,

a synchrotron which accelerates the bunches up to 120 GeV; in the Main Injector, several bunches are merged into one and used for the injection in the last stage.

The Fermilab accelerator complex works in supercycles of roughly 60 seconds in duration. The beam is split by electrostatic septa and delivered at different experimental halls all over the lab. A 120 GeV/c primary proton beam with variable intensity is extracted in four-second “spills” and sent to the Meson Center beam line.

LArIAT’s home at Fermilab is the Fermilab Test Beam Facility (FTBF), where the experiment characterizes a beam of charge particles downstream from the Meson Center beam line. Here, the primary beam is focused onto a tungsten target to create LArIAT’s secondary beam. The composition of the secondary particle beam is mainly positive pions. The momentum peak of the secondary beam was fixed at 64 GeV/c for the LArIAT data considered in this work, although the beam is tunable in momentum between 8-80 GeV/c; this configuration of the secondary beamline assured a stable beam delivery at the LArIAT experimental hall.

The secondary beam impinges then on a copper target within a steel collimator inside the LArIAT experimental hall (MC7) to create the LArIAT tertiary beam, (shown in Fig. 1.2). The steel collimator selects particles produced with a 13° production angle at the target down the beamline. The particles are then bent by 10° through a pair of dipole magnets. By configuring the field intensity of the magnets we allow the particles of LArIAT’s tertiary beam to span a momentum range from 0.2 to 1.4 GeV/c. The polarity of the magnet is also configurable and determines the sign of the beamline particles which are focused on the LArTPC. If the magnets polarity is positive the tertiary beam composition counts mostly pions and protons with a small fraction of electrons, muons, and kaons. It is the job of the LArIAT beamline detectors to select the particles polarity, to perform particle identification in the beamline and to measure the momentum of the tertiary beam particles before they get to the LArTPC. The LArIAT detectors are described in the following paragraphs.

Fermilab Accelerator Complex

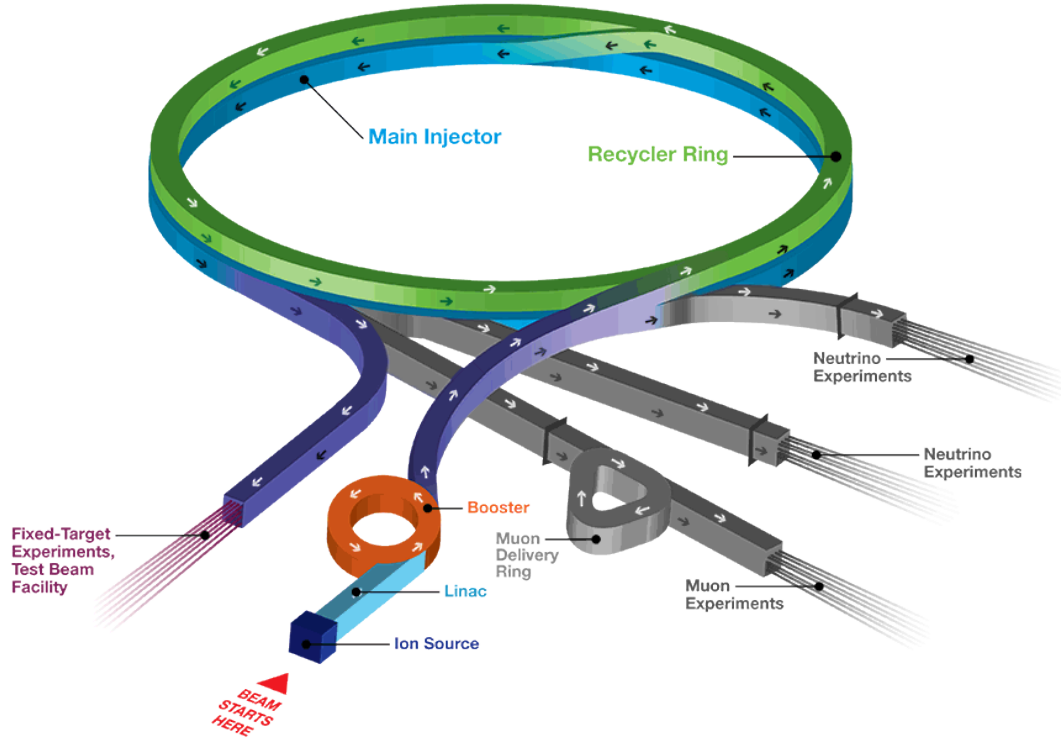


Figure 1.1: Layout of Fermilab Acellerator complex.

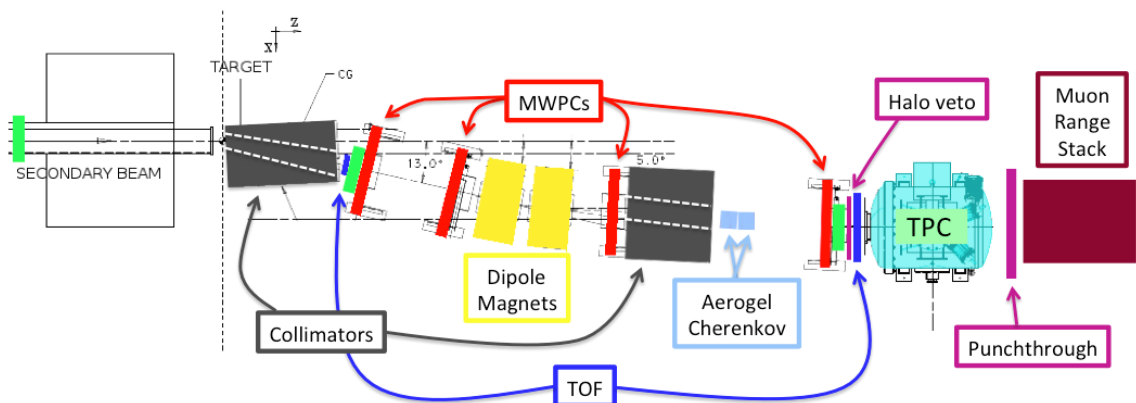


Figure 1.2: Bird's eye view of the LArIAT tertiary beamline. In grey: upstream and downstream collimators; in yellow: bending magnets; in red: wire chambers; in blue: time of flight; in green: liquid argon TPC volume; in maroon: muon range stack.

1.2 LArIAT Tertiary Beam Instrumentation

The instrumentation of LArIAT tertiary beam and the TPC components have changed several times during the three years of LArIAT data taking. The following paragraphs describe the components operational during “Run II”, the data taking period relevant to the hadron cross section measurements.

The key components of the tertiary beamline instrumentation for the hadron cross section analyses are the two bending magnets, a set of four wire chambers (WCs) and two time-of-flight scintillating paddles (TOF) and, of course, the LArTPC. The magnets determine the polarity of the particles in the tertiary beam; the combination of magnets and wire chambers determines the particles’ momentum, which is used to determine the particle species in conjunction with the TOF. A muon range stack downstream from the TPC and two sets of cosmic paddles configured as a telescope surrounding the TPC are also used for calibration purposes.

1.2.1 Bending Magnets

LArIAT uses a pair of identical Fermilab type “NDB” electromagnets, recycled from the Tevatron’s anti-proton ring, in a similar configuration used for the MINERvA T-977 test beam calibration [9]). The magnets are a fundamental piece of the LArIAT beamline equipment, as they are used for both particle identification and momentum measurement before the LArTPC. The sign of the current in the magnets allows us to select either positively or negatively charged particles; the value of the magnetic field is used in the momentum determination and in the subsequent particle identification.

We describe here the characteristics and response of one magnet, as the second one has a similar response, given its identical shape and history. Each magnet is a box with a rectangular aperture gap in the center to allow for the particle passage. The magnet aperture measures 14.224 cm in height, 31.75 cm in width, and 46.67 cm in length.

Since the wire chambers aperture ($\sim 12.8 \text{ cm}^2$) is smaller than the magnet aperture, only the central part of the magnet gap is utilized. The field is extremely uniform over this limited aperture and was measured with two hall probes, both calibrated with nuclear magnetic resonance probes. The probes measured the excitation curve shown in Figure 1.3.

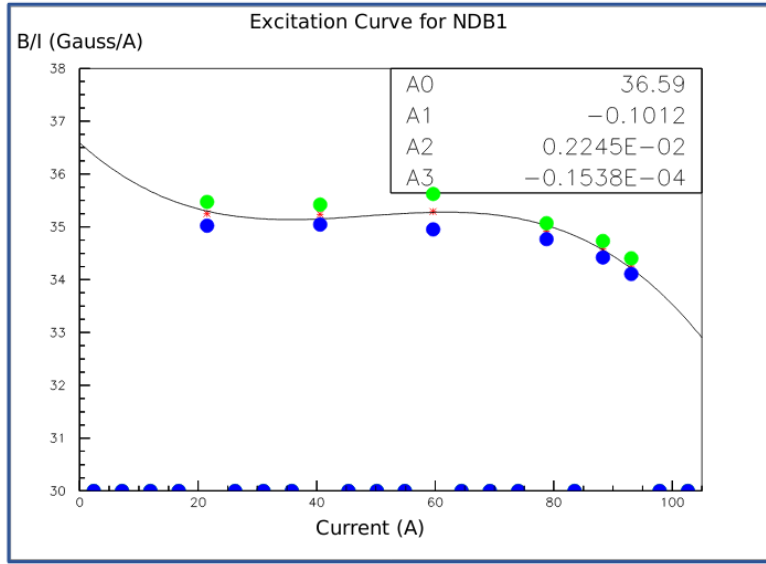


Figure 1.3: Magnetic field over current as a function of the current, for one NDB magnet (excitation curve). The data was collected using two hall probes (blue and green). We fit the readings with a cubic function (black) to average of measurements (red) given in the legend.

The current through the magnets at a given time is identical in both magnets. For the Run II data taking period, the current settings explored were 60A ($B \sim 0.21 \text{ T}$) and 100A ($B \sim 0.35 \text{ T}$) in both polarities. Albeit advantageous to enrich the tertiary beam composition with high mass particles such as kaons, we never pushed the magnets current over 100 A, not to incur in overheating. During operation, we operated a air and water cooling system on the magnets and we remotely monitored the magnets temperature.



Figure 1.4: One of the four Multi Wire Proportional Chambers (WC) used in the LArIAT tertiary beamline and relative read-out electronics.

1.2.2 Multi-Wire Proportional Chambers

LArIAT uses four multi-wire proportional chambers, or wire chambers (WC) for short, two upstream and two downstream from the bending magnets. The geometry of one chamber is shown in Figure 1.4: the WC effective aperture is a square of 12.8 cm perpendicular to the beam direction. Inside the chamber, the 128 horizontal and 128 vertical wires hang at a distance of 1 mm from each other in a mixture of 85% Argon and 15% isobutane gas. The WC operating voltage is between 2400 V and 2500 V. The LArIAT wire chambers are an upgraded version of the Fenker Chambers [11], where an extra grounding improves the signal to noise ratio of the electronic readout.

Two ASDQ chips [17] mounted on a mother board plugged into the chamber serve as front end amplifier/discriminator. The chips are connected to a multi-hit TDC [14] which provides a fast OR output used as first level trigger. The TDC time resolution is 1.18 ns/bin and can accept 2 edges per 9 ns. The maximum event rate acceptable by the chamber system is of 1 MHz: this rate is not a limiting factor considering that **the rate of the tertiary particle beam at the first wire chamber is estimated to be less than 15 kHz**. A full spill of data occurring once per supercycle is stored on the TDC board memory at once and read out by a specially designed controller. We use LVDS cables to carry both power and data between the controller and the TDCs and from

the controller to the rest of the DAQ.

Multi-Wire Proportional Chambers functionality

We use the wire chamber system together with the bending magnets to measure the particle's momentum.

In the simplest scenario, only one hit on each and every of the four wire chambers is recorded during a single readout of the detector systems. Thus, we use the hit positions in the two wire chambers upstream of the magnets to form a trajectory before the bend, and the hit positions in the two wire chambers downstream of the magnets to form a trajectory after the bend. We use the angles in the XZ plane between the upstream and downstream trajectories to calculate the Z component of the momentum as follows:

$$P_z = \frac{B_{eff}L_{eff}}{3.3(\sin(\theta_{DS}) - \sin(\theta_{US}))}, \quad (1.1)$$

where B_{eff} is the effective maximum field in a square field approximation, L_{eff} is the effective length of both magnets (twice the effective length of one magnet), θ_{US} is the angle off the z axis of the upstream trajectory, θ_{DS} is the angle off the z axis of the downstream trajectory and $3.3 c^{-1}$ is the conversion factor from [T·m] to [MeV/c]. By using the hit positions on the third and fourth wire chamber, we estimate the azimuthal and polar angles of the particle trajectory, and we are able to calculate the other components of the momentum.

The presence of multiple hits in a single wire chamber or the absence of hits in one (or more) wire chambers can complicate this simple scenario. The first complication is due to beam pile up, while the latter is due to wire chamber inefficiency. In the case of multiple hits on a single WC, at most one wire chamber track is reconstructed per event. Since the magnets bend particles only in the X direction, we assume the particle trajectory to be roughly constant in the YZ plane, thus we keep the

combination of hits which fit best with a straight line. It is still possible to reconstruct the particle’s momentum even if the information is missing in either of the two middle wire chambers (WC2 or WC3), by constraining the particle trajectory to cross the plane in between the magnets.

Events satisfying the simplest scenario of one single hit in each of the four wire chambers form the “Picky Track” sample. We construct another, higher statistics sample, where we loosen the requirements on single hit and wire chamber efficiency: the “High Yield” sample. For LArIAT Run II, the High Yield sample is about three times the Picky Tracks statistics. For the first measurements of the LArIAT hadronic cross section, we use the Picky Tracks sample because the uncertainty on the momentum is smaller and the comparison with the beamline MC results is straightforward compared with the High Yield sample; a possible future update and cross check of these analysis would be the use of the High Yield sample.

Four point track momentum uncertainty

1.2.3 Time-of-Flight System

Two scintillator paddles, one upstream to the first set of WCs and one downstream to the second set of WCs form LArIAT time-of-flight (TOF) detector system.

The upstream paddle is made of a 10 x 6 x 1 cm scintillator piece, read out by two PMTs mounted on the beam left side which collect the light from light guides mounted on all four edges of the scintillator. The downstream paddle is a 14 x 14 x 1 cm scintillator piece read out by two PMTs on the opposite ends of the scintillator. The relatively thin width on the beamline direction minimizes energy loss of the particles coming from the target in the scintillator material.

The CAEN 1751 digitizer is used to digitize the TOF PMTs signals at a sampling rate of 1 GHz. The 12 bit samples are stored in a circular memory buffer. At trigger time, data from the TOF PMTs are recorded to output in a 28.7 μ s windows starting

approximately 8.4 μ s before the trigger time.

TOF functionality

The TOF signals rise time (10-90%) is 4 ns and a full width, half-maximum of 9 ns consistent in time. The signal amplitudes from the upstream TOF and downstream TOF are slightly different: 200 mV for the upstream PMTs but only 50 mV for downstream PMTs. The time of the pulses was calculated utilizing an oversampled template derived from the data itself. We take the pulse pedestal from samples far from the pulse and subtract it to the pulse amplitude. We then stretch vertically a template to match the pedestal-subtracted pulse amplitude and we move it horizontally to find the time. With this technique, we find a pulse time-pickoff resolution better than 100 ps. The pulse pile up is not a significant problem given the TOF timing resolution and the rate of the particle beam. Leveraging on the pulses width uniformity of any given PMT, we flag events where two pulses overlap as closely in time as 4 ns with an 90% efficiency according to simulation.

We combine the pulses from the two PMTs on each paddle to determine the particles' arrival time by averaging the time measured from the single PMT, so to minimize errors due to optical path differences in the scintillator. However, a time spread of approximately 300 ps is present in both the upstream and downstream detectors, likely due to transit time jitter in the PMTs themselves. There is no evidence of systematic timing drift over long data-taking periods such as 3-4 months: the maximum variation of the average time differences between pairs of PMTs reading out the same scintillator is of the order of 150 ps.

1.2.4 Punch-Through and Muon Range Stack Instruments

The punch-thorough and the muon range stack (MuRS) detectors are located downstream of the TPC. These detectors provide a sample of TPC crossing tracks without



Figure 1.5: Image of the down stream time of flight paddle, PMTs and relative support structure before mounting.

relying on TPC information and can be used to improve particle ID for muons and pions with momentum higher than 450 MeV/c.

The punch-thorough is simple sheet of scintillator material, read out by two PMTs. The MuRS is a segmented block of steel with four slots instrumented with scintillation bars. The four steel layers in front of each instrumented slot are 2 cm, 2 cm, 14 cm and 16 cm wide in the beam direction. Each instrumented slot is equipped with four scintillation bars each, positioned horizontally in the direction orthogonal to the beam. Each scintillator bar measures $\text{?} \times \text{?} \times 2$ cm and it is read out by one PMT.

The signals from both the punch-thorough and the MuRS PMTs are digitized in the CAEN V1740, same as the TPC; the details of this discriminator are laid out in 1.3.2. It is worth noticing that the sampling time of the CAEN V1740 is slow (of the order of 128 ns), so pulse shape information from the PMT is lost. Punch-thorough and MuRS hits are formed utilizing the digital discriminator signals under threshold at a given time, where we obtain the threshold for each PMT directly on data distributions.

1.2.5 LArIAT Cosmic Ray Paddle Detectors

LArIAT triggers both on beam events and on cosmic rays events. We perform this latter trigger by using two sets of cosmic ray paddle detectors (a.k.a. “cosmic towers”.) The cosmic towers frame the LArIAT cryostat, as one sits in the downstream left corner and the other sits in the upstream right corner of the cryostat. Two paddle sets of four scintillators pieces each make up each cosmic tower, an upper set and a lower set per tower. Of the four paddles, a couple of two matched paddles stands upright while the a second matched pair lies across the top of the assembly in the top sets (or across the bottom of the assembly in the bottom sets). The horizontal couple is used as a veto for particles traveling from inside the TPC out. The four signals from the vertical paddles along one of the body diagonals of the TPC are combined in a logical “AND”. This allows to select cosmic muons crossing the TPC along one of its diagonals. Cosmic ray tracks crossing both anode and cathode populate the events triggered this way. This particularly useful sample of tracks (which we can safely assume to be associated with 5 GeV muons) can be used for many tasks; for example, we use anode-cathode piercing tracks to cross check the TPC electric field on data (see Appendix A), to calibrate the charge response of the TPC wires for the full TPC volume and to measure the electron lifetime in the chamber (see section ??).

A Zener-diode Hamamatsu H5783 PMT collects the light from a wavelength-shifting optical fiber which runs along one of the long sides of each paddle. A custom-made PMT Amplifier and Discrimination (PAD) circuit mounted at one end of the paddle collects signals from the PMTs and sends them to the Control and Concentrator Unit (CCU). We use the same connection to power the PMT, control voltage and threshold, and output the PMT signal as logic ECL pulse. We retrieved the scintillation paddles from the decommissioning of the CDF detector at Fermilab and we used only the paddles with a counting efficiency greater than 95% and low noise at working

voltage. The measured trigger rate of the whole system is 0.032 Hz, corresponding to ~ 2 muons per minute.



Figure 1.6: Photograph of one of the scintillation counters used in the cosmic towers.

1.3 In the Cryostat

1.3.1 Cryogenics and Argon Purity

LArIAT repurposed the ArgoNeuT cryostat [4] in order to use it in a beam of charge particles, and added a new process piping and a new liquid argon filtration system in FTBF. Inside the LArIAT experimental hall, the cryostat sits on the beam of charge particles with its horizontal main axis oriented parallel to the beam.

Two volumes make up LArIAT cryostat, shown in Figure 1.7: the inner vessel and the outer vessel. Purified liquid argon fills the inner vessel, while the outer volume provides insulation through a vacuum jacket equipped with layers of aluminized mylar superinsulation. The inner vessel is a cylinder of 130 cm length and 6.2 cm diameter, containing about 550 L of LAr, corresponding to a mass of 0.76 ton. We run the signal cables for the LArTPC and the high voltage feedthrough through a “chimney” at the top and mid-length of the cryostat.

Given the different scopes of the ArgoNeuT and LArIAT detectors, we made

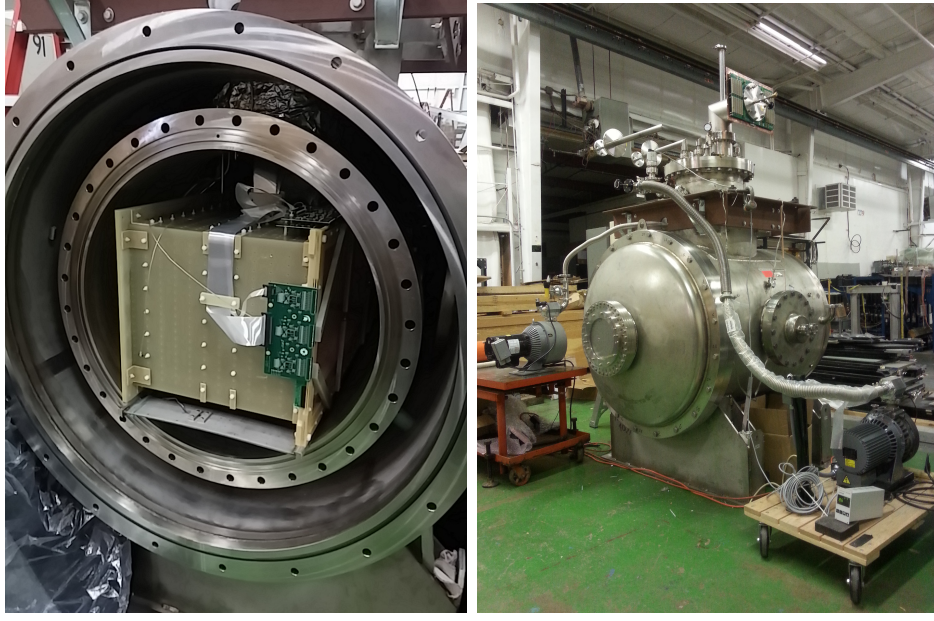


Figure 1.7: Left: the LArIAT TPC in the inner volume of the open cryostat. Right: cryostat fully sealed ready to be transported to FTBF.

several modification to the ArgoNeuT cryostat in order to use it in LArIAT. In particular, the modification shown in Figure 1.8 were necessary to account for the beam of charged particles entering the TPC and to employ the new FTBT liquid argon purification system. We added a “beam window” on the front outer end cap and an “excluder” on the inner endcap, with the scope of minimizing the amount of dead material upstream of the TPC’s active volume. Doing so, we reduced the amount of uninstrumented material before the TPC from ~ 1.6 radiation lengths (X_0) (ArgoNeuT) to less than $0.3 X_0$ (LArIAT). To allow studies of the scintillation light, we added a side port feedthrough which enables the mounting of the light collection system, as well as the connections for the corresponding signal and high-voltage cables (see Section 1.3.3). We modified the bottom of the cryostat adding Conflat and ISO flange sealing to connect the liquid argon transfer line to the new argon cooling and purification system.

As in any other LArTPC, argon purity is a crucial parameter for LArIAT. Indeed, the presence of contaminants effects both the basic working principles of a LArTPC,



Figure 1.8: Main modifications to the ArgoNeuT cryostat: 1) outlet for connection to the purification system at the bottom of the cryostat; 2) the “beam-window” on the outer endcap and “excluder” which reduce the amount of non-instrumented material before the TPC; 3) the side port to host the light collection system.

as shown in section 0.1.2: electronegative contaminants such as oxygen and water decrease the number of ionization electrons collected on the wires after drifting through the volume. In addition, contaminants such as Nitrogen decrease the light yield from scintillation light, especially in its slow component. In LArIAT, contaminations should not exceed the level of 100 parts per trillion (ppt). We achieve this level of purity in several stages. The specifics required for the commercial argon bought for LArIAT are 2 parts per million (ppm) oxygen, 3.5 ppm water, and 10 ppm nitrogen. This argon is monitored with the use of commercial gas analyzer. Argon is stored in a dewar external to LArIAT hall and filtered before filling the TPC. LArIAT uses a filtration system designed for the Liquid Argon Purity Demonstrator (LAPD) [10]: half of a 77 liter filter contains a 4A molecular sieve (Sigma-Aldrich [21]) apt to remove mainly water, while the other half contains BASF CU-0226 S, a highly dispersed copper oxide impregnated on a high surface area alumina, apt to remove mainly oxygen [6]. A single pass of argon in the filter is sufficient to achieve the necessary

purity, unless the filter is saturated. In case the filter saturates, the media needs to be regenerated by using heated gas; this happened twice during the Run II period¹. The filtered argon reaches the inner vessel via a liquid feedthrough on the top of the cryostat. Argon is not recirculated in the system, rather it boils off and vent to the atmosphere. During data taking, we replenish the argon in the cryostat several times per day to keep the TPC high voltage feedthrough and cold electronics always submerged. In fact, we constantly monitor the level, temperature, and pressure of the argon both in the commercial dewar and inside the cryostat during data taking.

1.3.2 LArTPC: Charge Collection

The LArIAT Liquid Argon Time Projection Chamber is a rectangular box of dimensions 47 cm (width) x 40 cm (height) x 90 cm (length), containing 170 liters of Liquid Argon. The LArTPC three major subcomponents are

- 1) the cathode and field cage,
- 2) the wire planes,
- 3) the read-out electronics.

Cathode and field cage

A G10 plain sheet with copper metallization on one of the 40 x 90 cm inner surfaces forms the cathode. A high-voltage feedthrough on the top of the LArIAT cryostat delivers the high voltage to the cathode; scope of the high voltage system (Figure 1.9) is to drift ionization electrons from the interaction of charged particles in the liquid argon to the wire planes. The power supply used in this system is a Glassman LX125N16 [13] capable of generating up to -125 kV and 16 mA of current, but

1. We deemed the filter regeneration necessary every time the electron lifetime dropped under 100 μ s.

operated at -23.5kV during LArIAT Run-II. The power supply is connected via high voltage cables to a series of filter pots before finally reaching the cathode.

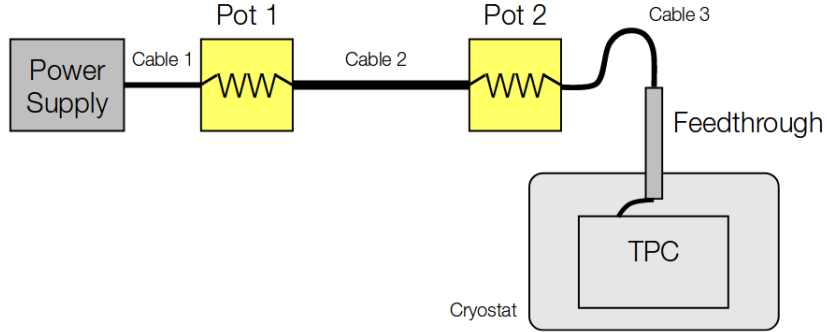


Figure 1.9: Schematic of the LArIAT high voltage system.

The field cage is made of twenty-three parallel copper rings framing the inner walls of the G10 TPC structure. A network of voltage-dividing resistors connected to the field cage rings steps down the high voltage from the cathode to form a uniform electric field. The electric field over the entire TPC drift volume is 486 V/cm (see A). The maximum drift length, i.e. the distance between cathode and anode planes, is 47 cm.

Wire planes

The wire planes measure the charge deposited in the TPC active volume. The drifting charge induces a current on the wire of the inner planes and it is collected on the collection plane wires. LArIAT counts three wire planes separated by 4 mm spaces: in order of increasing distance from the cathode, they are the shield, the induction and the collection plane. The “wire pitch”, i.e., the distance between two consecutive wires in a given plane, is 4 mm. The shield plane counts 225 parallel wires of equal length oriented vertically. This plane is not connected with the read-out electronics; rather it shields the outer planes from extremely long induction signals due to the ionization chamber in the whole drift volume. As the shield plane acts almost like a

Faraday cage, the shape of signals in the first instrumented plane (induction) results easier to reconstruct. Both the induction and collection planes count 240 parallel wires of different length oriented at 60° from the vertical with opposite signs. Electrons moving past the induction plane will induce a bipolar pulse on its wires; the drifting electrons will be then collected on the collection plane's wires, forming a unipolar pulse.

The three wire planes and the cathode form three drift volumes, as shown in Figure 1.10. The main drift volume is defined as the region between the cathode plane and the shield plane (C-S). The other two drift regions are those between the shield plane and the induction plane (S-I), and between the induction plane and the collection plane (I-C). The electric field in these regions is chosen to satisfy the charge transparency condition and allow for 100% transmission of the drifting electrons through the shield and the induction planes.

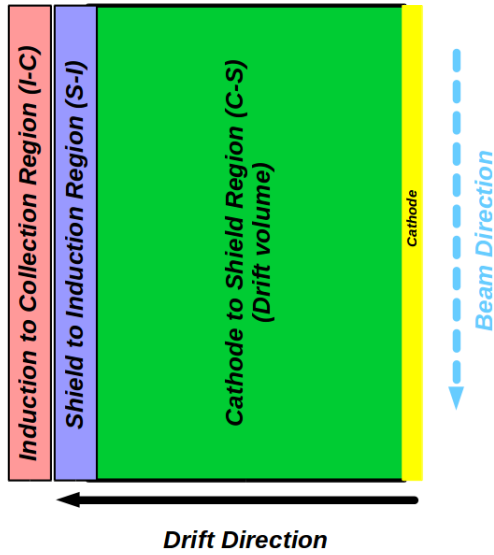


Figure 1.10: Schematic of the three drift regions inside the LArIAT TPC: the main drift volume between the cathode and the shield plane (C-S) in green, the region between the shield plane and the induction plane (S-I) in purple, and the region between the induction plane and the collection plane (I-C) in pink.

Table 1.1 provides the default voltages applied to the cathode and the shield,

induction, and collection plane.

Table 1.1: Cathode and anode planes default voltages

Cathode	Shield	Induction	Collection
-23.17 kV	-298.8 V	-18.5 V	338.5 V

Electronics

Dedicated electronics read the induction and collection plane wires, for a total of 480-channel analog signal path from the TPC wires to the signal digitizers. A digital control system for the TPC-mounted electronics, a power supply, and a distribution system complete the front-end system. Figure 1.11 shows a block diagram of the overall system. The direct readout of the ionization electrons in liquid argon forms typically small signals on the wires, which need amplification in order to be processed. LArIAT performs the amplification stage directly in cold with amplifiers mounted on the TPC frame inside the liquid argon, achieving a remarkable Signal-to-Noise ratio. The signal from the ASICs are driven to the other end of the readout chain, to the CAEN V1740 digitizers. The CAEN V1740 has a 12 bit resolution and a maximum input range of 2 VDC, resulting in about 180 ADC count for a crossing MIP.

1.3.3 LArTPC: Light Collection System

The collection of scintillation photons is the second mechanism of particle detection in argon other than the ionization electrons. Over the course of LArIAT’s three years of data taking, the light collection system changed several times. We describe here the light collection system for Run II. Two PMTs, a 3-inch diameter Hamamatsu R-11065 and 2-inch diameter ETL D757KFL [3], as well as three SiPMs arrays (two Hamamatsu S11828-3344M 4x4 arrays and one single-channel SensL MicroFB-60035) are mounted on the PEEK support structure. PEEK screws into an access flange

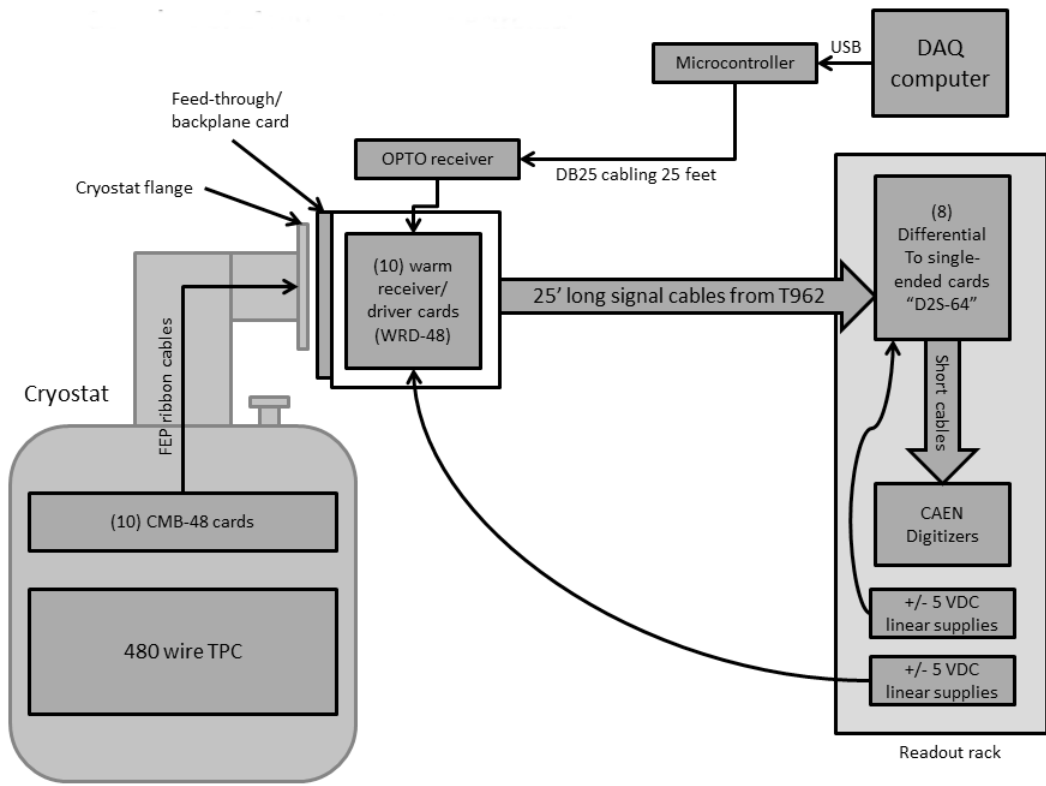


Figure 1.11: Overview of LArIAT Front End electronics.

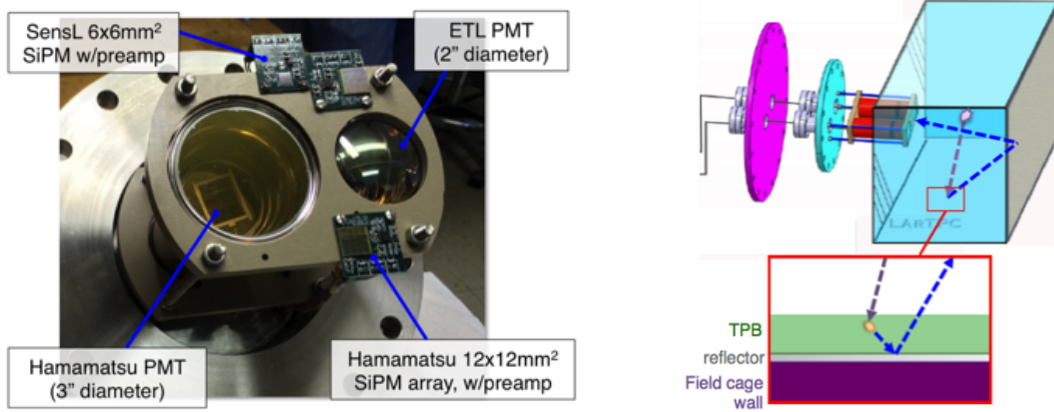


Figure 1.12: LArIAT’s photodetector system for observing LAr scintillation light inside the TPC (left), and a simplified schematic of VUV light being wavelength-shifting along the TPB-coated reflecting foils (right).

as shown in Figure 1.12, on the anode side, leaving approximately 5 cm of clearance from the collection plane.

Liquid argon scintillates in vacuum-ultraviolet (VUV) range at 128 nm; since cryogenic PMTs are not sensitive to VUV wavelengths, we need to shift the light in a region visible to the PMTs. In LArIAT, the wavelength shifting is achieved by installing on the four walls of the TPC highly-reflective VIKUITY dielectric substrate foils coated with a thin layer of tetraphenyl-butadiene (TPB). The scintillation light interaction with the TPC emits one or more visible photons, we are then reflected into the chamber. Thus, the light yield increases and results more uniform across the TPC active volume, allowing the possibility of light-based calorimetry, currently under study.

For Run II, we coated both the windows of the ETL PMT and SensL SiPM with a thin layer of TPB. In doing so, some of the VUV scintillation light converts into visible right at the sensor faces, keeping information on the direction of the light source. Information about the light directionality is lost for light reflected on foils, as the reflection is uniform in angle.

1.4 Trigger and DAQ

The LArIAT DAQ and trigger system governs the read out of all the many subsystems forming LArIAT. The CAEN V1495 module and its user-programmable FPGA are the core of this system. Every 10 ns, this module checks for matches between sixteen logical inputs and user-defined patterns in the trigger menu; if it finds a match for two consecutive clock ticks, that trigger fires.

LArIAT receives three logic from the Fermilab accelerator complex related to the beam timing which we use as input triggers: a pulse just before the beam, a pulse indicating beam-on, and a beam-off pulse.

The beam instruments, the cosmic ray taggers, and the light collection system provide the other NIM-standard logic pulse inputs to the trigger decision. We automatically log the trigger inputs configuration with the rest of the DAQ configuration at the beginning of each run.

Fundamental inputs to the trigger card come from the TOF (see Sec. 1.2.3) and the wire chambers (see Sec. 1.2.2), as activity in these systems points to the presence of a charged particle in tertiary beam line. In particular, the discriminated pulses from the TOF PMTs form a NIM logic pulse for the trigger logic. We ask for a coincidence within a 20 ns window for all the pulses from the PMTs looking at the same scintillator block and use the coincidence between the upstream and downstream paddle to inform the trigger decision. In order to form a coincidence between the upstream and downstream paddles, we delay the upstream paddle coincidence by 20 ns and widen it by 100 ns. The delay and widening are necessary to account for both lightspeed particles and slower particles (high-mass) to travel the 6.5 m between the upstream and the downstream paddles. For the read out of the wire chambers, we use a total of sixteen multi-hit TDCs, four per chamber: two TDC per plane (horizontal and vertical), sixty-four wires per TDC. In each TDC, we keep the logical “OR” for any signal over threshold from the sixty-four wires. We then require a

coincidence between the “OR” for the horizontal TDCs and the “OR” for the vertical TDCs: with this logic we make sure that at least one horizontal wire and one vertical wire saw significant signal in one wire chamber. The single logical pulse from each of the four wire chambers feeds into the first four inputs to the V1495 trigger card. We require a coincidence within 20 ns of at least three logical inputs to form a trigger.

The cosmic towers (see Section 1.2.5) provide another primary input to the trigger, in order to capture long tracks from cosmic muons crossing the TPC. We use NIM modules to require coincidences between one upper and one lower paddle set of any opposite cosmic towers. The OR all the opposite towers’ coincidences is fed as an input to the trigger card.

We use the signal from the cryogenic PMTs (see Section ??) to form several interesting triggers. The coincidence of signal from all the PMT pulses within \sim 20 ns is an indication of ionizing radiation in the TPC and forms a trigger input. The coincidence of two subsequent scintillation logic pulses delayed by a maximum of $7\ \mu\text{s}$ forms the Michel electron trigger.

1.5 Control Systems

LArIAT is a complex ensemble of systems which needed to be monitored at once during data taking. We performed the monitoring of the systems operations with a slow control system, a DAQ monitoring system and a low level data quality monitoring described in the following sections.

Slow Control

We used the Synoptic Java Web Start framework as a real-time display of subsystem conditions. Its simple Graphical User Interface allowed us to change the operating parameters and to graph the trends of several variables of interest for all the tertiary

beam detectors. Among the most important quantities monitored by Synoptic there are the level of argon in both the inner vessel and the external dewar, the operating voltages of cathode and wire planes, of the PMTs and SiPMs, and of the four wire chambers, as well as the magnets temperature. Figure 1.13 shows an example of the monitoring system. LArIAT uses the Accelerator Control NETwork system (ACNET) to monitor the beam conditions of the MCenter beamline. For example, the horizontal and vertical position of the beam at the first two wire chambers (WC1 and WC2) are shown in 1.14 as seen by the shifter during data taking.

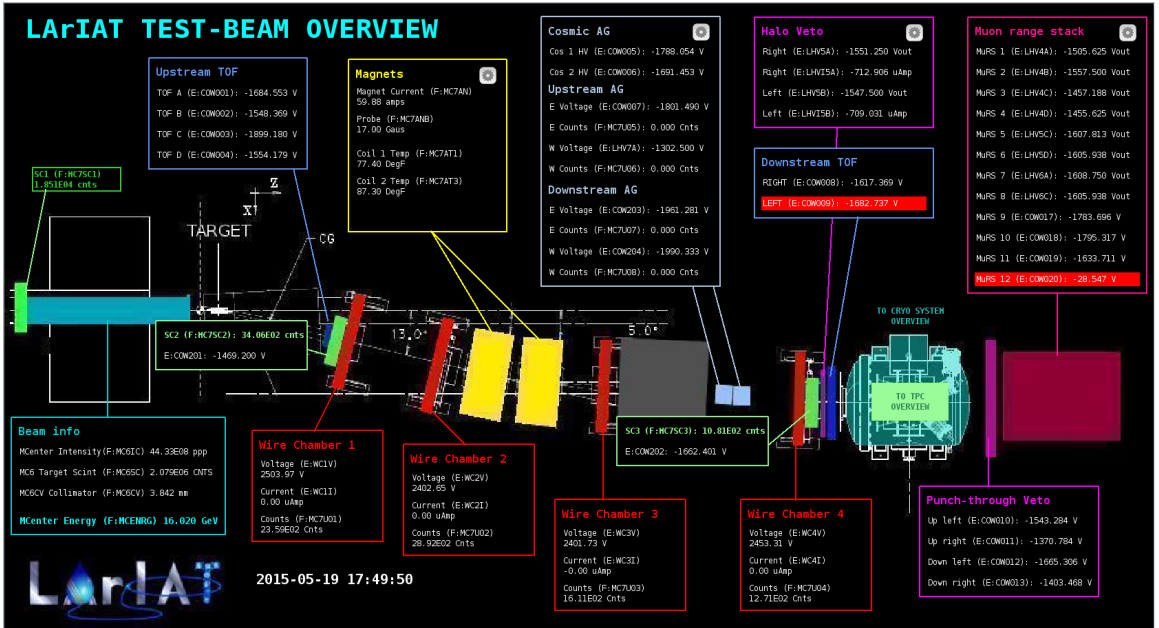


Figure 1.13: Interface of the Synoptic slow control system

DAQ Monitoring

We monitor the data taking and the run time evolution with the Run Status Webpage (<http://lariat-wbm.fnal.gov/lariat/run.html>), a webpage updated in real-time. The page displays, among other information, the total number of triggers in the event, the total number of detectors triggered during a beam spill, the trigger patterns, the number of times a particular trigger pattern was satisfied during a beam spill, and

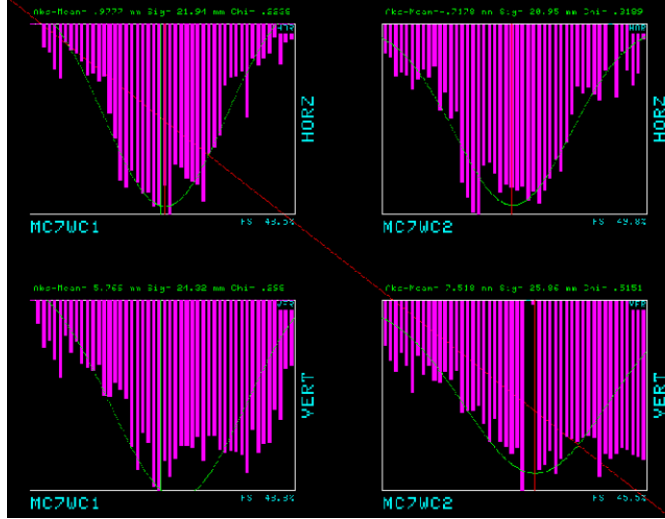


Figure 1.14: Beam position at the upstream wire chambers monitored with ACNET.

the current time relative to the Fermilab accelerator complex supercycle. A screen shot of the page is show in figure 1.15.

Data Quality Monitoring

We employ two systems to ensure the quality of our data during data taking: the Near-Real-Time Data Quality Monitoring and the Event Viewer.

The Near-Real-Time Data Quality Monitoring (DQM) is a webpage which receives updates from all the VME boards in the trigger system and displays the results of a quick analysis of the DAQ stream of raw data on a spill-by-spill basis. The DQM allows the shifter to monitor almost in real time (typically with a 2-minute delay) a series of low level-quantities and compare them to past collections of beam spills. Some of the variables monitored in the DQM are the pedestal mean and RMS on CAEN digitizer boards of the TPC wires and PMTs of the beamline detectors, the hit occupancy and timing plots on the wire chambers, and number of data fragments recorded that are used to build a TPC event. Abnormal values for low-level quantity in the data activate a series of alarms in the DQM; this quick feedback on the DAQ and beam conditions is fundamental to assure a fast debugging of the detector and a

very efficient data taking during beam uptime.

The online Event Viewer displays a two dimensional representation of LArIAT TPC events on both the Induction and the Collection planes in near real time. The raw pulses collected by the DAQ on each wire are plotted as a function of drift time, resulting in an image of the TPC event easily readable by the shifter. This tool guarantees a particularly good check of the TPC operation which activate an immediate feedback for troubleshooting a number of issues. For example, it is easy for the shifter to spot high occupancy events and request a reduction of the primary beam intensity, or to spot a decrease of the argon purity which requires the regeneration of filters, or to catch the presence of electronic noise and reboot the ASICs. An example of high occupancy event is shown in 1.16.

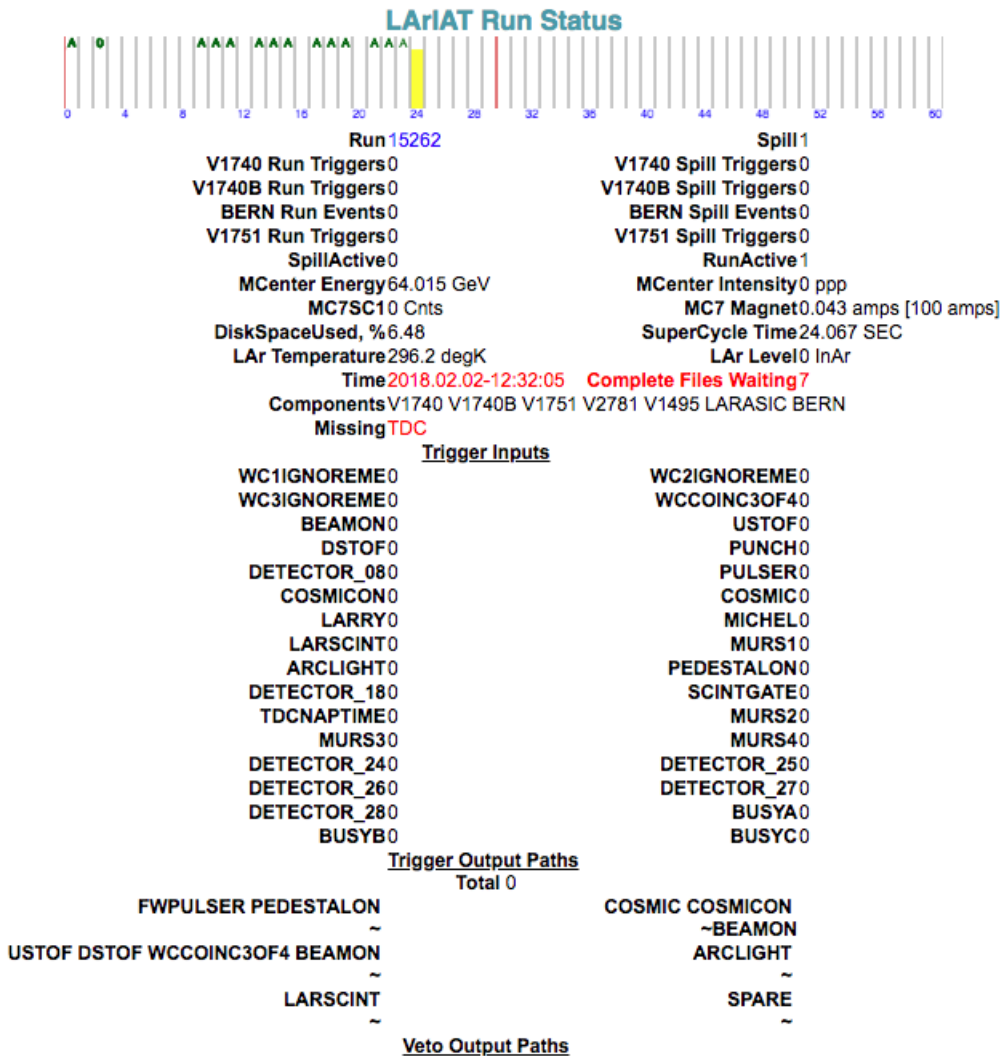


Figure 1.15: Run Status page at LArIAT downtime. At the top the yellow bar displays the current position in the Fermilab supercycle. Interesting information to be monitored by the shifter were the run number and number of spills, time elapsed from data taking (here in red), the energy of the secondary beam and the trigger paths.

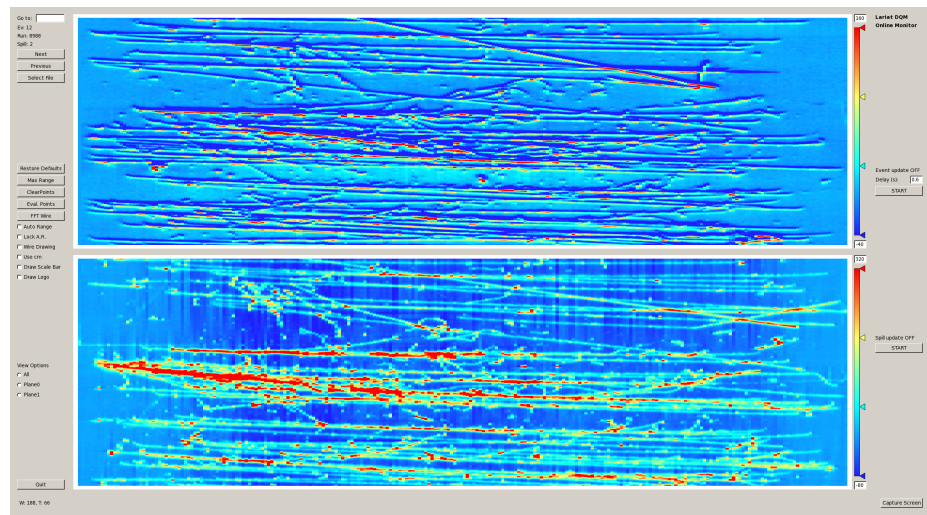


Figure 1.16: High occupancy event display: induction plane (top) and collection plane (bottom).

Chapter 2

Hadron Interactions in Argon: Cross Section

2.1 How to Measure a Hadron Cross Section in LArIAT

We use both the LArIAT beamline detectors and the LArTPC information to measure hadronic cross sections in argon. Albeit with small differences, both the π^- - Ar and K^+ - Ar total hadronic cross section measurements rely on the same procedure described in details in the following paragraphs: we select the particle of interest using a combination of beamline detectors and TPC information (paragraph 2.1.1), we perform a handshake between the beamline information and the TPC tracking to assure we are selecting the right TPC track (paragraph 2.1.2), and we apply the “thin slice” method to get to the final result (paragraph 2.1.3). We show a cross check of this method in paragraph 2.1.4.

2.1.1 Event Selection

Beamline events

As will be clear in paragraph 2.1.3, beamline particle identification and momentum measurement before entering the TPC are fundamental information for the hadronic cross sections measurements in LArIAT. Thus, we scan the LArIAT data to keep only events whose wire chamber and time of flight information is registered. Additionally, we perform a check of the plausibility of the trajectory inside the beamline detectors: given the position of the hits in the four wire chambers, we make sure the particle trajectory does not cross any impenetrable material such as the collimator and the magnets steel.

Particle Identification in the beamline

In data, the main tool to establish the identity of the hadron of interest is the LArIAT tertiary beamline, in its function of mass spectrometer. We combine the measurement of the time of flight, TOF , and the beamline momentum, p_{Beam} , to reconstruct the invariant mass of the particles in the beamline, m_{Beam} , as follows

$$m_{Beam} = \frac{p_{Beam}}{c} \sqrt{\left(\frac{TOF * c}{l}\right)^2 - 1}, \quad (2.1)$$

where c is the speed of light and l is the length of the particle trajectory between the time of flight paddles.

Figure 2.1 shows the mass distribution for the Run II negative polarity runs on the left and positive polarity runs on the right. We perform the classification of events into the different samples as follows:

- π, μ, e : $0 \text{ MeV} < \text{mass} < 350 \text{ MeV}$
- kaon: $350 \text{ MeV} < \text{mass} < 650 \text{ MeV}$

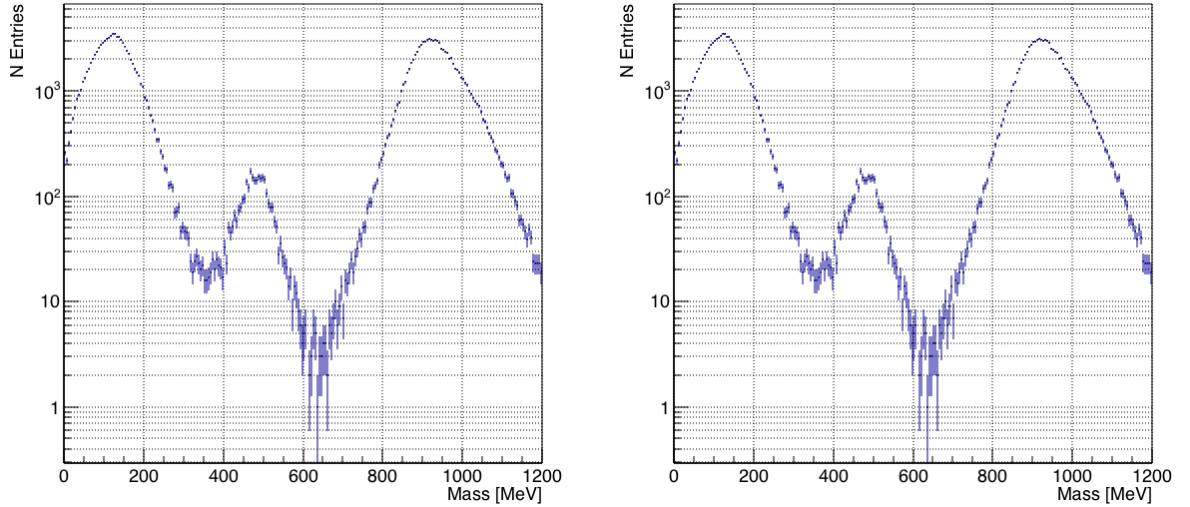


Figure 2.1: The mass plotted for a sample of Run-II events reconstructed in the beamline, negative polarity runs on the left and positive polarity runs on the right. The classification of the events into π , μ , e , kaon, or proton is based on this distribution.
CHANGE PLOTS

- proton: $650 \text{ MeV} < \text{mass} < 3000 \text{ MeV}$.

Additional Particle Identification technique

In the case of the π^- -Ar cross section, the resolution of beamline mass spectrometer is not sufficient to select a beam of pure pions. In fact, muons and electrons survive the selection on the beamline mass value. It is important to notice that the composition of the negative polarity beam is mostly pions, as discussed in ???. Anyhow, we devise a selection on the TPC information to mitigate the presence of electrons in the sample used for the pion cross section. The selection relies on the different topologies of a pion and an electron event in the argon: while the former will trace a track inside the TPC active volume, the latter will tend to “shower”, i.e. interact with the medium, produce bremsstrahlung photons which pair convert into several short tracks. We provide details of this selection in section ??.

Pile up mitigation

The secondary beam impinging on LArIAT secondary target produces a plethora of particles. The presence of upstream and downstream collimators greatly abates the number of particles tracing down the LArIAT beamline. However, more than one beamline particles, or particles produced from the beam interaction with the beamline detectors, may sneak into the LArTPC during its readout time. The TPC readout is triggered by the actual particle firing the beamline detectors; we call “pile up” the additional traces in the TPC. We adjusted the primary beam intensity between LArIAT Run I and Run II to minimize the presence of events with high pile up particles in the data sample. For the cross section analyses, we remove events with more than 4 tracks in the first 14 cm upstream portion of the TPC from the sample.

probably need to do a better job explaining pile up

2.1.2 Wire Chamber to TPC Match

For each event passing the selection on its beamline information we need to identify the track inside the TPC corresponding to the particle which triggered the beamline detectors, a procedure we refer to as “WC to TPC match” (WC2TPC for short). In general, the TPC tracking algorithm will reconstruct more than one track in the event, partially due to the fact that hadrons interact in the chamber, as shown in figure ??, and partially because of pile up particles during the triggered TPC drift time, as shown in figure ??.

ADD EVENT DISPLAYS

We attempt to uniquely match one wire chamber track to one and only one reconstructed TPC track. In data, this match leverages on a geometrical selection exploiting both the position of the wire chamber and TPC tracks, and the angle between them. We consider only TPC tracks whose first point is in the first 2 cm upstream portion of the TPC for the match. We project the wire chamber track to the TPC front face where we define the x_{FF} and y_{FF} coordinates used for evaluating

the match. We define ΔX as the difference between the x position of the most upstream point of the TPC track and x_{FF} . ΔY is defined analogously. We define the radius difference, ΔR , as $\Delta R = \sqrt{\Delta X^2 + \Delta Y^2}$. The angle between the incident WC track and the TPC track in the plane that contains them defines α . If $\Delta R < 4$ cm, $\alpha < 8^\circ$, a match between WC-track and TPC reconstructed track is found. We describe how we determinate the best value for the radius and angular selection in sec ???. In MC, we mimic the matching between the WC and the TPC track by constructing a fake WC track using truth information at wire chamber four. We then apply the same WC to TPC matching algorithm as in data. We discard events with multiple WC2TPC matches. We use only TPC track matched to WC tracks in the cross section calculation.

2.1.3 The Thin Slice Method

Cross Sections on Thin Target

Cross section measurements on a thin target have been the bread and butter of nuclear and particle experimentalists since the Rutherford experiments NEED CITATION. At their core, this type of experiments consists in shooting a beam of particles with a known flux on a thin target and recording the outgoing flux.

In general, the target is not a single particle, but rather a slab of material containing many diffusion centers. The so-called “thin target” approximation assumes that the target centers are uniformly distributed in the material and that the target is thin compared to the interaction length so that no center of interaction sits in front of another. In this approximation, the ratio between the number of particles interacting in the target $N_{Interacting}$ and number of incident particles $N_{Incident}$ determines the interaction probability $P_{Interacting}$, which is the complementary to one of the survival

probability $P_{Survival}$. Equation 2.2

$$P_{Survival} = 1 - P_{Interacting} = 1 - \frac{N_{Interacting}}{N_{Incident}} = e^{-\sigma_{TOT} n \delta X} \quad (2.2)$$

describes the probability for a particle to survive the thin target. This formula relates the total cross section σ_{TOT} , the density of the target centers n and the thickness of the target along the incident hadron direction δX , to the interaction probability¹. If the target is thin compared to the interaction length of the process considered, we can Taylor expand the exponential function in equation 2.2 and find a simple proportionality relationship between the number of incident and interacting particles, and the cross section, as shown in equation 2.3:

$$1 - \frac{N_{Interacting}}{N_{Incident}} = 1 - \sigma_{TOT} n \delta X + O(\delta X^2). \quad (2.3)$$

Solving for the cross section, we find:

$$\sigma_{TOT} = \frac{1}{n \delta X} \frac{N_{Interacting}}{N_{Incident}}. \quad (2.4)$$

Not-so-Thin Target: Slicing the Argon

The LArIAT TPC, with its 90 cm of length, is not a thin target. Find expected interaction length for hadrons and kaons. However, the fine-grained tracking of the LArIAT LArTPC allows us to treat the argon volume as a sequence of many adjacent thin targets.

As described in section 1, LArIAT wire planes count 240 wires each. The wires are oriented at +/- 60° from the vertical direction at 4 mm spacing, while the beam direction is oriented 3 degrees off the z axis in the XZ plane. review this math The

¹. The scattering center density in the target, n , relates to the argon density ρ , the Avogadro number N_A and the argon molar mass m_A as $n = \frac{\rho N_A}{m_A}$.

wires collect signals proportional to the energy loss of the hadron along its path in a $\delta X = 4 \text{ mm}/\sin(60^\circ) \approx 4.7 \text{ mm}$ slab of liquid argon. Thus, one can think to slice the TPC into many thin targets of $\delta X = 4.7 \text{ mm}$ thickness along the direction of the incident particle.

Considering each slice j a “thin target”, we can apply the cross section calculation from Eq. 2.4 iteratively, evaluating the kinetic energy of the hadron as it enters each slice, E_j^{kin} . For each WC-to-TPC matched particle, the energy of the hadron entering the TPC is known thanks to the momentum and mass determination by the tertiary beamline,

$$E_{FrontFace}^{kin} = \sqrt{p_{Beam}^2 - m_{Beam}^2} - m_{Beam} - E_{loss}, \quad (2.5)$$

where E_{loss} is a correction for the energy loss in the dead material between the beamline and the TPC front face (more on ??). The energy of the hadron at the each slab is determined by subtracting the energy released by the particle in the previous slabs. For example, at the j^{th} point of a track, the kinetic energy will be

$$E_j^{kin} = E_{FrontFace}^{kin} - \sum_{i < j} \Delta E_i, \quad (2.6)$$

where ΔE_i is the energy deposited at each argon slice before the j^{th} point as measured by the calorimetry associated with the tracking.

If the particle enters a slice, it contributes to $N_{Incident}(E^{kin})$ in the energy bin corresponding to its kinetic energy in that slice. If it interacts in the slice, it then also contributes to $N_{Interacting}(E^{kin})$ in the appropriate energy bin. The cross section as a function of kinetic energy, $\sigma_{TOT}(E^{kin})$ will then be proportional to the ratio $\frac{N_{Interacting}(E^{kin})}{N_{Incident}(E^{kin})}$.

The statistical uncertainty for each energy bin is calculated by error propagation from the statistical uncertainty on $N_{Incident}$ and $N_{Interacting}$. Since the number of

incident hadrons in each energy bin is given by a simple counting, we assume that $N_{Incident}$ is distributed as a poissonian with mean and σ^2 equal to $N_{Incident}$ in each bin. On the other hand, $N_{Interacting}$ follows a binomial distribution: a particle in a given energy bin might or might not interact. The square of the variance for the binomial is given by

$$\sigma^2 = \mathcal{N}P_{Interacting}(1 - P_{Interacting}); \quad (2.7)$$

since the interaction probability $P_{Interacting}$ is $\frac{N_{Interacting}}{N_{Incident}}$ and the number of tries \mathcal{N} is $N_{Incident}$, equation 2.7 translates into

$$\sigma^2 = N_{Incident} \frac{N_{Interacting}}{N_{Incident}} \left(1 - \frac{N_{Interacting}}{N_{Incident}}\right) = N_{Interacting} \left(1 - \frac{N_{Interacting}}{N_{Incident}}\right). \quad (2.8)$$

$N_{Incident}$ and $N_{Interacting}$ are not independent. The uncertainty on the cross section is thus calculated as

$$\delta\sigma_{tot}(E) = \sigma_{tot}(E) \left(\frac{\delta N_{Interacting}}{N_{Interacting}} + \frac{\delta N_{Incident}}{N_{Incident}} \right) \quad (2.9)$$

where:

$$\delta N_{Incident} = \sqrt{N_{Incident}} \quad (2.10)$$

$$\delta N_{Interacting} = \sqrt{N_{Interacting} \left(1 - \frac{N_{Interacting}}{N_{Incident}}\right)}. \quad (2.11)$$

2.1.4 Procedure testing with truth quantities

The π^- -Ar and K^+ -Ar total hadronic cross section implemented in Geant4 can be used as a tool to validate the measurement methodology. We describe here a closure test done on Monte Carlo to prove that the methodology of slicing the TPC retrieves the underlying cross section distribution implemented in Geant4 within the statistical error.

For pions in the considered energy range, the Geant4 inelastic model adopted to is “BertiniCascade”, while the elastic model “hElasticLHEP”. For kaons, the Geant4 inelastic model adopted to is “BertiniCascade”, while the elastic model “hElasticLHEP”.

For the validation test, we fire about 390000 pions and 140000 kaons inside the LArIAT TPC active volume using the DDMC (see sec ??). We apply the thin-sliced method on using true quantities to calculate the hadron kinetic energy at each slab in order to decouple reconstruction effects to eventual issues with the methodology. For each slab of 4.7 mm length on the path of the hadron, we integrate the true energy deposition as given by the Geant4 transportation model. Then, we recursively subtracted it from the hadron kinetic energy at the TPC front face to evaluate the kinetic energy at each slab until the true interaction point is reached. Doing so, we obtain the true interacting and incident distributions for the considered hadron and we obtain the true MC cross section as a function of the hadron true kinetic energy.

Figure ?? shows the total hadronic cross section for argon implemented in Geant4 10.01.p3 (solid lines) overlaid with the true MC cross section as obtained with the sliced TPC method (markers) for pions on the left and kaons on the right; the total cross section is shown in green, the elastic cross section in blue and the inelastic cross section in red. The nice agreement with the Geant4 distribution and the cross section obtained with the sliced TPC method gives us confidence in the validity of the methodology.

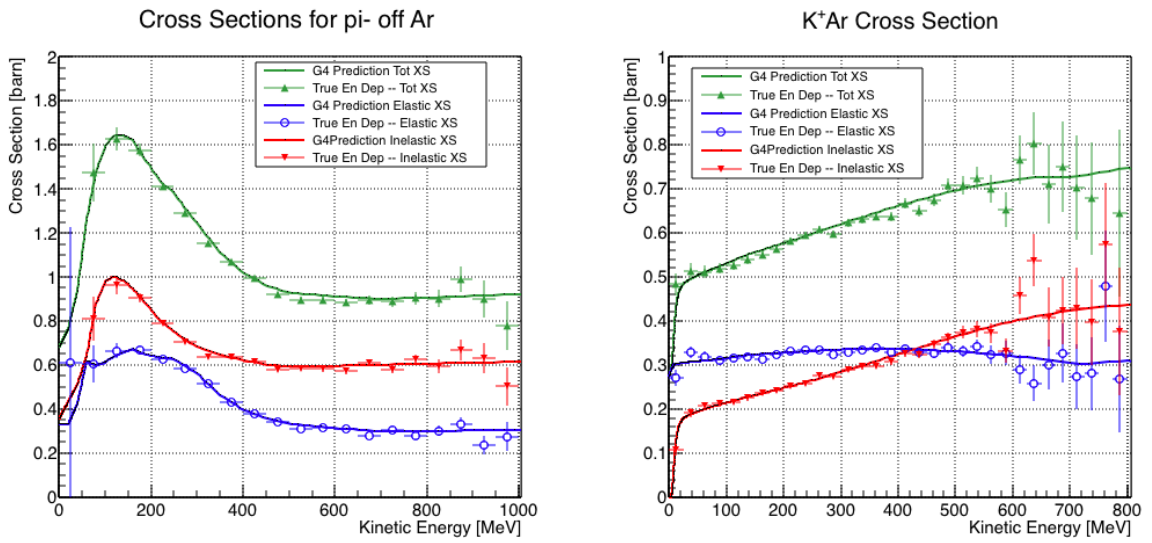


Figure 2.2: Hadronic cross sections for π^- -Ar (left) and K^+ -Ar (right) implemented in Geant4 10.01.p3 (solid lines) overlaid the true MC cross section as obtained with the sliced TPC method (markers). The total cross section is shown in green, the elastic cross section in blue and the inelastic cross section in red.

Appendix A

Measurement of LArIAT Electric Field

The electric field of a LArTPC in the drift volume is a fundamental quantity for the proper functionality of this technology, as it affects almost every reconstructed quantity such as the position of hits or their collected charge. Given its importance, we calculate the electric field for LArIAT with a single line diagram from our HV circuit and we cross check the obtained value with a measurement relying only on TPC data.

Before getting into the details of the measurement procedures, it is important to explicit the relationship between some quantities in play. The electric field and the drift velocity (v_{drift}) are related as follows

$$v_{drift} = \mu(E_{field}, T)E_{field}, \quad (\text{A.1})$$

where μ is the electron mobility, which depends on the electric field and on the temperature (T). The empirical formula for this dependency is described in [?] and shown in Figure A.1 for several argon temperatures.

The relationship between the drift time (t_{drift}) and the drift velocity is trivially

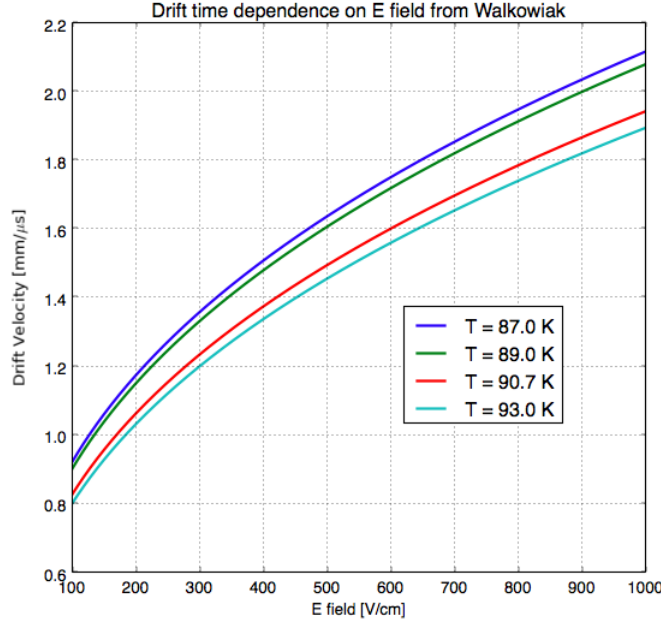


Figure A.1: Drift velocity dependence on electric field for several temperatures. The slope of the line at any one point represents the electron mobility for that given temperature and electric field.

Table A.1: Electric field and drift velocities in LArIAT smaller drift volumes

	Shield-Induction	Induction-Collection
E_{filed}	700.625 V/cm	892.5 V/cm
v_{drift}	1.73 mm/μs	1.90 mm/μs
t_{drift}	2.31 μs	2.11 μs

given by

$$t_{drift} = \Delta x / v_{drift}, \quad (\text{A.2})$$

where Δx is the distance between the edges of the drift region. Table A.1 reports the values of the electric field, drift velocity, and drift times for the smaller drift volumes.

With these basic parameters established, we can now move on to calculating the electric field in the main drift region (between the cathode and the shield plane).

Single line diagram method

The electric field strength in the LArIAT main drift volume can be determined knowing the voltage applied to the cathode, the voltage applied at the shield plane, and the distance between them. We assume the distance between the cathode and the shield plane to be 470 mm and any length contraction due to the liquid argon is negligibly small (~ 2 mm).

The voltage applied to the cathode can be calculated using Ohm's law and the single line diagram shown in Figure A.2. A set of two filter pots for emergency power dissipation are positioned between the Glassman power supply and the cathode, one at each end of the feeder cable, each with an internal resistance of $40 \text{ M}\Omega$. The output current of the Glassman power supply is then used to determine the electric field strength. Figure A.3 shows an average current of 0.004172 mA from the Glassman power supply.

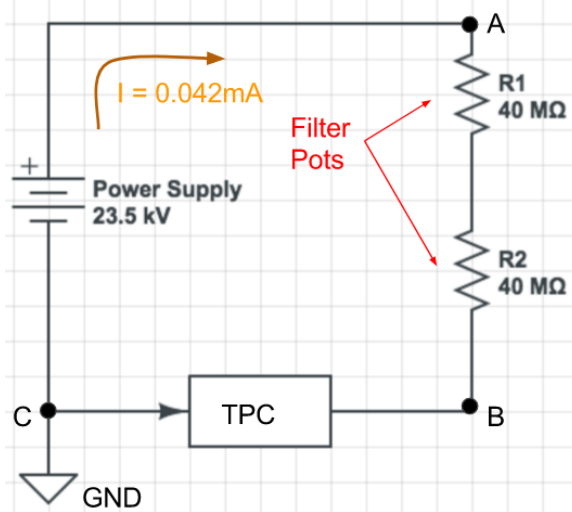


Figure A.2: get rid of current line LArIAT HV simple schematics.

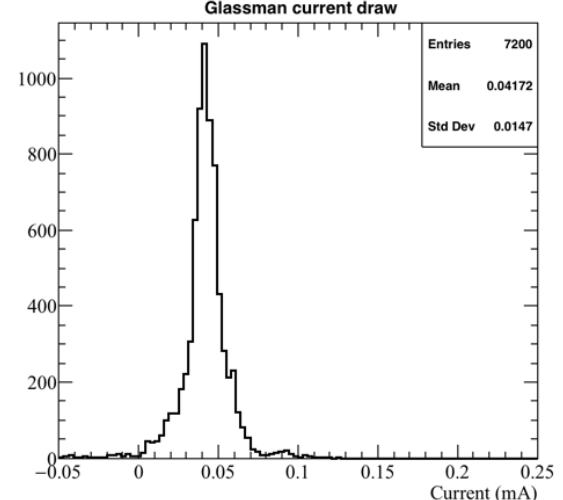


Figure A.3: **the axis is wrong!!** Current reading from the Glassman between May 25th and May 30th, 2016 (typical Run-II conditions).

Using this current, the voltage at the cathode is calculated as

$$V_{BC} = V_{PS} - (I \times R_{eq}) = -23.5 \text{ kV} + (0.00417 \text{ mA} \times 80 \text{ M}\Omega) = -23.17 \text{ kV}, \quad (\text{A.3})$$

where I is the current and R_{eq} is the equivalent resistor representing the two filter pots. The electric field, drift voltage, and drift time are then calculated to be

$$E_{\text{field}} = \frac{V_{BC} - V_{\text{shield}}}{\Delta x} = 486.54 \text{ V/cm} \quad (\text{A.4})$$

E field using cathode-anode piercing tracks

We devise an independent method to measure the drift time (and consequently drift velocity and electric field) using TPC cathode to anode piercing tracks. We use this method as a cross check to the single line method. The basic idea is simple:

0. Select cosmic ray events with only 1 reconstructed track
1. Reduce the events to the one containing tracks that cross both anode and cathode
2. Identify the first and last hit of the track
3. Measure the time difference between these two hits (Δt).

This method works under the assumptions that the time it takes for a cosmic particle to cross the chamber ($\sim \text{ns}$) is small compared to the charge drift time ($\sim \text{hundreds of } \mu\text{s}$).

We choose cosmic events to allow for a high number of anode to cathode piercing tracks (ACP tracks), rejecting beam events where the particles travel almost perpendicularly to drift direction. We select events with only one reconstructed track to maximize the chance of selecting a single crossing muon (no-michel electron). We utilize ACP tracks because their hits span the full drift length of the TPC, see figure

A.4, allowing us to define where the first and last hit of the tracks are located in space regardless of our assumption of the electric field.

One of the main features of this method is that it doesn't rely on the measurement of the trigger time. Since Δt is the time difference between the first and last hit of a track and we assume the charge started drifting at the same time for both hits, the measurement of the absolute beginning of drift time t_0 is unnecessary. We boost the presence of ACP tracks in the cosmic sample by imposing the following requirements on tracks:

- vertical position (Y) of first and last hits within ± 18 cm from TPC center (avoid Top-Bottom tracks)
- horizontal position (Z) of first and last hits within 2 and 86 cm from TPC front face (avoid through going tracks)
- track length greater than 48 cm (more likely to be crossing)
- angle from the drift direction (phi in figure A.5) smaller than 50 deg (more reliable tracking)
- angle from the beam direction (theta in figure A.5) grater than 50 deg (more reliable tracking)

Tracks passing all these selection requirements are used for the Δt calculation.

For each track passing our selection, we loop through the associated hits in order to retrieve the timing information. The analysis is performed separately on hits on the collection plane and induction plane, but lead to consistent results. As an example of the time difference, figures A.6 and A.7 represent the difference in time between the last and first hit of the selected tracks for Run-II Positive Polarity sample on the collection and induction plane respectively. We fit with a Gaussian to the peak of the Δt distributions to extract the mean drift time and the uncertainty associated with

it. The long tail at low Δt represent contamination of non-ACP tracks in the track selection. We apply the same procedure to Run-I and Run-II, positive and negative polarity alike.

To convert Δt recorded for the hits on the induction plane to the drift time we utilize the formula

$$t_{drift} = \Delta t - t_{S-I} \quad (\text{A.5})$$

where t_{drift} is the time the charge takes to drift in the main volume between the cathode and the shield plane and t_{S-I} is the time it takes for the charge to drift from the shield plane to the induction plane. In Table A.1 we calculated the drift velocity in the S-I region, thus we can calculate t_{S-I} as

$$t_{S-I} = \frac{l_{S-I}}{v_{S-I}} = \frac{4mm}{1.745mm/\mu s} \quad (\text{A.6})$$

where l_{S-I} is the distance between the shield and induction plane and v_{S-I} is the drift velocity in the same region. A completely analogous procedure is followed for the hits on the collection plane, taking into account the time the charge spent in drifting from shield to induction as well as between the induction and collection plane. The value for Δt_{drift} , the calculated drift velocity (v_{drift}), and corresponding drift electric field for the various run periods is given in Table A.2 and are consistent with the electric field value calculated with the single line diagram method.

Delta t_{drift} , drift v and E field with ACP tracks

Data Period	Δt_{Drift} [μs]	Drift velocity [mm/ μs]	E field [V/cm]
RunI Positive Polarity Induction	311.1 ± 2.4	1.51 ± 0.01	486.6 ± 21
RunI Positive Polarity Collection	310.9 ± 2.6	1.51 ± 0.01	487.2 ± 21
RunII Positive Polarity Induction	315.7 ± 2.8	1.49 ± 0.01	467.9 ± 21
RunII Positive Polarity Collection	315.7 ± 2.7	1.49 ± 0.01	467.9 ± 21
RunII Negative Polarity Induction	315.9 ± 2.6	1.49 ± 0.01	467.1 ± 21
RunII Negative Polarity Collection	315.1 ± 2.8	1.49 ± 0.01	470.3 ± 21
Average Values	314.1	1.50 ± 0.01	474.3 ± 21

Table A.2: Δt for the different data samples used for the Anode-Cathode Piercing tracks study.

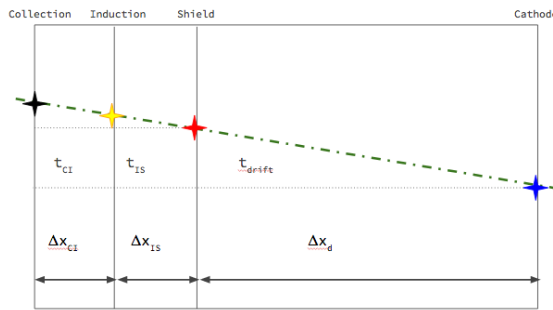


Figure A.4: Pictorial representation of the YX view of the TPC. The distance within the anode planes and between the shield plane and the cathode is purposely out of proportion to illustrate the time difference between hits on collection and induction. A ACP track is shown as an example.

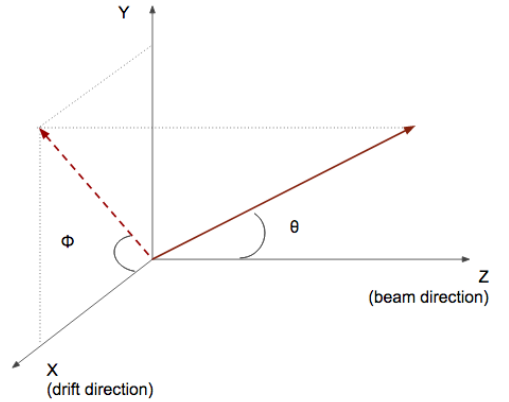


Figure A.5: Angle definition in the context of LArIAT coordinates system.

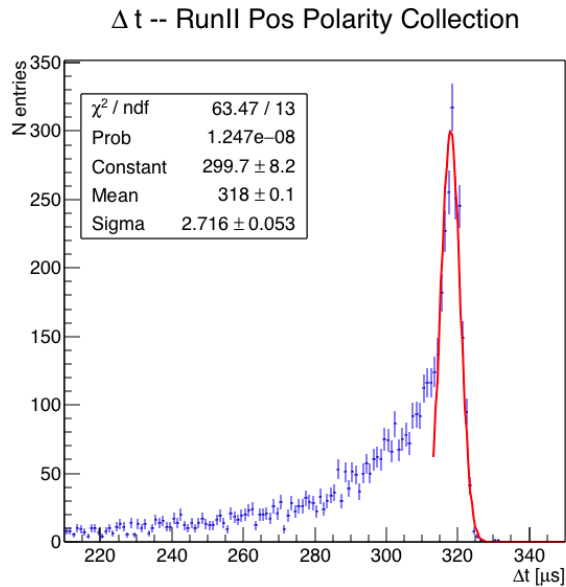


Figure A.6: Collection plane Δt fit for Run II positive polarity ACP data selected tracks.

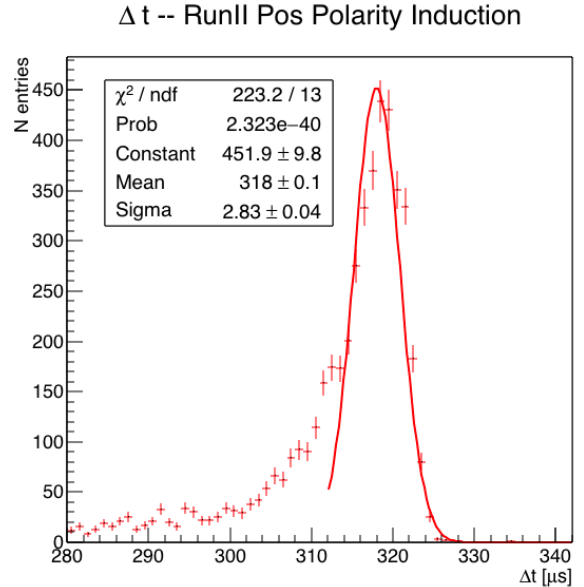


Figure A.7: Induction plane Δt fit for Run II positive polarity ACP data selected tracks.

Bibliography

- [1] R Acciarri, C Adams, J Asaadi, B Baller, T Bolton, C Bromberg, F Cavanna, E Church, D Edmunds, A Ereditato, S Farooq, B Fleming, H Greenlee, G Horton-Smith, C James, E Klein, K Lang, P Laurens, D McKee, R Mehdiyev, B Page, O Palamara, K Partyka, G Rameika, B Rebel, M Soderberg, J Spitz, A M Szelc, M Weber, M Wojcik, T Yang, and G P Zeller. A study of electron recombination using highly ionizing particles in the argoneut liquid argon tpc. *Journal of Instrumentation*, 8(08):P08005, 2013.
- [2] R Acciarri, M Antonello, B Baibussinov, M Baldo-Ceolin, P Benetti, F Calaprice, E Calligarich, M Cambiaghi, N Canci, F Carbonara, F Cavanna, S Centro, A G Cocco, F Di Pompeo, G Fiorillo, C Galbiati, V Gallo, L Grandi, G Meng, I Modena, C Montanari, O Palamara, L Pandola, G B Piano Mortari, F Pietropaolo, G L Raselli, M Roncadelli, M Rossella, C Rubbia, E Segreto, A M Szelc, S Ventura, and C Vignoli. Effects of nitrogen contamination in liquid argon. *Journal of Instrumentation*, 5(06):P06003, 2010.
- [3] R. Acciarri et al. Demonstration and Comparison of Operation of Photomultiplier Tubes at Liquid Argon Temperature. *JINST*, 7:P01016, 2012.
- [4] C. Anderson et al. The ArgoNeuT Detector in the NuMI Low-Energy beam line at Fermilab. *JINST*, 7:P10019, 2012.

- [5] M. Antonello, B. Baibussinov, P. Benetti, E. Calligarich, N. Canci, S. Centro, A. Cesana, K. Cieslik, D. B. Cline, A. G. Cocco, A. Dabrowska, D. Dequal, A. Dermenev, R. Dolfini, C. Farnese, A. Fava, A. Ferrari, G. Fiorillo, D. Gibin, S. Gninenko, A. Guglielmi, M. Haranczyk, J. Holeczek, A. Ivashkin, J. Kisiel, I. Kochanek, J. Lagoda, S. Mania, A. Menegolli, G. Meng, C. Montanari, S. Otwinowski, A. Piazzoli, P. Picchi, F. Pietropaolo, P. Plonski, A. Rapoldi, G. L. Raselli, M. Rossella, C. Rubbia, P. Sala, A. Scaramelli, E. Segreto, F. Sergiampietri, D. Stefan, J. Stepaniak, R. Sulej, M. Szarska, M. Terrani, F. Varanini, S. Ventura, C. Vignoli, H. Wang, X. Yang, A. Zalewska, and K. Zaremba. Precise 3d track reconstruction algorithm for the ICARUS t600 liquid argon time projection chamber detector. *Advances in High Energy Physics*, 2013:1–16, 2013.
- [6] BASF Corp. 100 Park Avenue, Florham Park, NJ 07932 USA.
- [7] S.E. Derenzo, A.R. Kirschbaum, P.H. Eberhard, R.R. Ross, and F.T. Solmitz. Test of a liquid argon chamber with 20 m rms resolution. *Nuclear Instruments and Methods*, 122:319 – 327, 1974.
- [8] A Ereditato, C C Hsu, S Janos, I Kreslo, M Messina, C Rudolf von Rohr, B Rossi, T Strauss, M S Weber, and M Zeller. Design and operation of argontube: a 5 m long drift liquid argon tpc. *Journal of Instrumentation*, 8(07):P07002, 2013.
- [9] L. Aliaga et al. Minerva neutrino detector response measured with test beam data. *Nuclear Instruments and Methods in Physics Research Section A: Accelerators, Spectrometers, Detectors and Associated Equipment*, 789:28 – 42, 2015.
- [10] M Adamowski et al. The liquid argon purity demonstrator. *Journal of Instrumentation*, 9(07):P07005, 2014.

- [11] H Fenker. Standard beam pwc for fermilab. Technical report, Fermi National Accelerator Lab., Batavia, IL (USA), 1983.
- [12] V.M. Gehman, S.R. Seibert, K. Rielage, A. Hime, Y. Sun, D.-M. Mei, J. Maassen, and D. Moore. Fluorescence efficiency and visible re-emission spectrum of tetraphenyl butadiene films at extreme ultraviolet wavelengths. *Nuclear Instruments and Methods in Physics Research Section A: Accelerators, Spectrometers, Detectors and Associated Equipment*, 654(1):116 – 121, 2011.
- [13] Glassman High Voltage, Inc., Precision Regulated High Voltage DC Power Supply.
- [14] S. Hansen, D. Jensen, G. Savage, E. Skup, and A. Soha. Fermilab test beam multi-wire proportional chamber tracking system upgrade. June 2014. International Conference on Technology and Instrumentation in Particle Physics (TIPP 2014).
- [15] H J Hilke. Time projection chambers. *Reports on Progress in Physics*, 73(11):116201, 2010.
- [16] B J P Jones, C S Chiu, J M Conrad, C M Ignarra, T Katori, and M Toups. A measurement of the absorption of liquid argon scintillation light by dissolved nitrogen at the part-per-million level. *Journal of Instrumentation*, 8(07):P07011, 2013.
- [17] FM Newcomer, S Tedja, R Van Berg, J Van der Spiegel, and HH Williams. A fast, low power, amplifier-shaper-discriminator for high rate straw tracking systems. *IEEE Transactions on Nuclear Science*, 40(4):630–636, 1993.
- [18] D. R. Nygren. The time projection chamber: A new 4π detector for charged particles. Technical report, 1974.

- [19] C. Patrignani et al. Review of Particle Physics. *Chin. Phys.*, C40(10):100001, 2016.
- [20] C. Rubbia. The Liquid Argon Time Projection Chamber: A New Concept for Neutrino Detectors. 1977.
- [21] Sigma-Aldrich, P.O. Box 14508, St. Louis, MO 63178 USA.
- [22] N Yahlali, L M P Fernandes, K Gonzlez, A N C Garcia, and A Soriano. Imaging with sipms in noble-gas detectors. *Journal of Instrumentation*, 8(01):C01003, 2013.